INTERNATIONAL JOURNAL FOR NUMERICAL METHODS IN ENGINEERING
Int. J. Numer. Meth. Engng 2008; **74**:1162–1197
Published online 13 November 2007 in Wiley InterScience (www.interscience.wiley.com). DOI: 10.1002/nme.2205

Variational r-adaption in elastodynamics

M. G. Zielonka, M. Ortiz*, † and J. E. Marsden

Division of Engineering and Applied Science, California Institute of Technology, Pasadena, CA 91125, U.S.A.

SUMMARY

We develop a variational r-adaptive finite element framework for solid dynamic applications and explore its conceptual links with the theory of dynamic configurational forces. The central idea underlying the proposed approach is to allow Hamilton's principle of stationary action to determine jointly the evolution of the displacement field and the discretization of the reference configuration of the body. This is accomplished by rendering the action stationary with respect to the material and spatial nodal coordinates simultaneously. However, we find that a naive consistent Galerkin discretization of the action leads to intrinsically unstable solutions. Remarkably, we also find that this unstable behavior is eliminated when a mixed, multifield version of Hamilton's principle is adopted. Additional features of the proposed numerical implementation include the use of uncoupled space and time discretizations; the use of independent space interpolations for velocities and deformations; the application of these interpolations over a continuously varying adaptive mesh; and the application of mixed variational integrators with independent time interpolations for velocities and nodal parameters. The accuracy, robustness and versatility of the approach are assessed and demonstrated by way of convergence tests and selected examples. Copyright © 2007 John Wiley & Sons, Ltd.

Received 23 April 2007; Revised 27 August 2007; Accepted 29 August 2007

KEY WORDS: variational methods; mesh adaption; elastodynamics

1. INTRODUCTION

This work is concerned with the exploration and development of a *variational finite element mesh adaption* framework for non-linear solid *dynamics* and its conceptual links with the concept of *dynamic configurational forces*. The distinctive attribute of this methodology is that the underlying variational principle, namely, Hamilton's principle of stationary action, governs *both* the evolution discretized fields *and* the mesh on which the discretization is defined.

*Correspondence to: M. Ortiz, Division of Engineering and Applied Science, California Institute of Technology, Pasadena, CA 91125, U.S.A.
†E-mail: ortiz@aero.caltech.edu

Contract/grant sponsor: Department of Energy
Contract/grant sponsor: NSF-ITR; contract/grant number: ACI-0204932

Dynamic solutions may exhibit moving discontinuities, and it is sometimes advantageous to adapt the resolution of the computational grid so as to resolve the discontinuities with a minimum degrees of freedom. For linear-elliptic problems, a natural adaption strategy consists of optimizing the mesh so that an error bound is minimized. This strategy may formally be extended to dynamics and finite deformations by recourse to time discretization and linearization [1], but in this case the coercivity of the linearized energy norm and the regularity of the solution can no longer be guaranteed in general. The existence, uniqueness and regularity properties of solutions in non-linear elastodynamics are not completely understood at present and the entire conceptual framework of *energy-norm errors* and *error bounds* as a basis for mesh adaption simply collapses in that setting.

An alternative approach that applies naturally to non-linear variational problems and generalizes the conventional energy-norm error framework for linear problems is to *rely on the variational principle to supply both the solution and the optimal mesh*. This approach is *error-estimate free* and thus applies with great generality to strongly non-linear problems for which error estimation is not possible. For static problems, the concept of using the underlying variational principle to optimize the discretization enjoys a long tradition dating back, at least, to [2–4] in the special context of structural and two-dimensional linearized elasticity. By contrast, the connection between mesh optimization and configurational or energetic forces (see [5, 6]) has only been recognized recently [7–14]. A variety of solution strategies have recently been proposed for static problems based on the notion of configurational equilibrium [8, 10, 11, 13, 15, 16], and the robustness and scope of the approach have been demonstrated in a number of areas of applications.

The objective of this paper is to extend the paradigm of variational mesh adaption to *dynamics*. In principle, this extension appears to be deceptively straightforward. Thus, for conservative dynamical systems, the governing variational principle is *Hamilton's principle of stationary action*. By adopting a space–time viewpoint, the notion of configurational force and configurational force balance can be extended to elastodynamics ([17–20] and references therein). It is readily verified that for a homogeneous body the equations of linear momentum balance and configurational force balance are not independent, but one follows from the other. However, the introduction of a discretization breaks the homogeneity of the body and the equations of linear momentum balance and configurational force balance, obtained by varying the action with respect to spatial and material nodal positions, become independent for general deformations. One may think of the equations of linear momentum balance as governing the motion of the spatial configuration and of the equations of configurational force balance as governing the motion of the mesh, although this intuition is somewhat misleading as both systems of equations are tightly coupled in general. In this variational approach, *both the motion and the evolution of the mesh render the action stationary and follow jointly from the governing variational principle*.

While the possibility of using configurational force equilibrium for mesh adaption in elastodynamics has been speculated within the past [17–21], only one actual implementation restricted to one-dimensional problems had been attempted to date [10]. However, in attempting a general implementation, an unexpected essential difficulty arises: *A direct space–time discretization of the action results in unstable discrete systems in general.* The resolution of this essential difficulty is critical to the feasibility and success of the approach. The instabilities that plague naive space–time discretizations may be traced to inaccuracies in the *velocity field* introduced by the motion of the mesh. In order to overcome this essential difficulty, we resort to a *mixed*, *multifield*, *version of Hamilton's principle* that allows for *independent* interpolation of velocities *and* deformations. This *mixed Hamilton's principle* is closely linked to the *Hamilton–Pontryagin*, *or HP*, *variational principle* (the principle incorporates extra fields in the same way as is done in optimal control

DOI: 10.1002/nme

theory and the Pontryagin maximum principle; see [22] and also [23] for a historical overview and the link with Dirac constraint theory and [24] for another application of the HP principle). It is also in the spirit of mixed methods in computational mechanics, which are derived from the de Veubeke–Hu–Washizu-mixed variational principle (see [25, 26]). Interestingly, *unlike the naive single-field formulation*, *when this mixed version of Hamilton's principle is used to determine the time evolution of nodal displacements*, *velocities and the mesh*, *the resulting solutions are found to be stable*.

This paper is structured as follows. In Section 2 we begin by illustrating the essential difficulty and its root cause by means of a simple one-dimensional example. The mixed action and Hamilton's principle are introduced in Section 3 in a semi-discrete setting. Time discretization is introduced in Section 5 by means of variational integrators. For simplicity, asynchronous time discretization is not considered since that degree of generality is not necessary to illustrate the main features of variational mesh adaption. Finally, a number of numerical examples are presented in Section 6 that demonstrate the increased accuracy and stability of scope of the method.

2. AN ILLUSTRATION OF THE ESSENTIAL DIFFICULTY

We proceed to illustrate the essential difficulty of variational r-adaption in dynamics by means of a simple one-dimensional example: a bar discretized into two linear elements. This example suffices to reveal a strikingly different behavior between a naive Galerkin reduction and the mixed formulation. In particular, the Galerkin formulation turns out to be unstable in an essential way.

2.1. One-dimensional vibrating bar

As a first illustrative example, we consider a one-dimensional body $B=[0, L]$ fixed on both sides and free of body forces. The deformation of the body over the time interval (t_0, t_f) is described globally by the deformation mapping $\varphi:[0, L]\times(t_0, t_f)\to\mathbb{R}$, and locally by the material velocity field $V(X, t)=\dot{\varphi}(X, t)$ and the deformation gradient $F(X, t)=\nabla\varphi(X, t)$. We assume that the body is homogeneous hyperelastic with total energy density $W(F)$ and that the mass density R is constant. The motion of the body is governed by Hamilton's principle of stationary action:

$$\delta S=0 \tag{1}$$

where

$$S(\varphi)=\int_{t_0}^{t_f} L(\varphi, \dot{\varphi})\,\mathrm{d}t \tag{2}$$

is the action of the body, and

$$L(\varphi, \dot{\varphi})=\int_0^L \left\{\frac{1}{2}R\dot{\varphi}^2(X, t)-W(F(X, t))\right\}\mathrm{d}X \tag{3}$$

is its Lagrangian. Alternatively, the trajectory and velocity field of the body follow simultaneously from the stationary condition:

$$\delta S^{\mathrm{mix}}=0 \tag{4}$$

DOI: 10.1002/nme

where

$$S^{\mathrm{mix}}(\varphi, V) = \int_{t_0}^{t_f} L^{\mathrm{mix}}(\varphi, V)\,\mathrm{d}t \tag{5}$$

is the mixed action of the body, and

$$L^{\mathrm{mix}}(\varphi, V) = \int_0^L \left\{ \frac{1}{2} R V^2(X,t) - W(F(X,t)) + RV(X,t)[\dot{\varphi}(X,t) - V(X,t)] \right\} \mathrm{d}X \tag{6}$$

its mixed action. In the preceding equation, the field V is assumed *a priori* to be independent from the *consistent* velocity field $\dot{\varphi}$. For now we simply remark that, evidently, the Euler–Lagrange equations corresponding to this mixed formulation are the equation of motion and the *a posteriori* identification of the assumed velocity with the consistent velocity field:

$$\frac{\mathrm{d}}{\mathrm{d}t}\{RV\} = \frac{\mathrm{d}}{\mathrm{d}X}\{DW(F)\}$$
$$V - \dot{\varphi} = 0$$

We shall return to this mixed principle in more generality in Section 3. Already Equation (6) has shown the similarity and difference with the HP principle: in the HP principle, the term $RV(X,t)$ on the right-hand side would be replaced with another field, namely, with P, the material momentum density. Varying V in the resulting HP principle equates P to RV and varying P produces the equation $V - \dot{\varphi} = 0$. The HP principle and the mixed action principle (6) are clearly analogous to the de Veubeke–Hu–Washizu principle, in which the field F is introduced as an independent variable and a term $\sigma \cdot (F - \nabla\varphi)$ is introduced in the variational principle, where now the 'Lagrange multiplier' σ, or the conjugate variable to F, is the stress.

2.1.1. Spatial discretization. The body is discretized into two piecewise linear finite elements with one internal free node. Both the nodal coordinate of the internal node in the deformed configuration $x_1(t)$ *and* its nodal coordinate in the reference configuration $X_1(t)$ are taken as unknowns. The corresponding interpolated deformation mapping is

$$\varphi_h(X,t) = \begin{cases} \dfrac{X}{X_1(t)} x_1(t) & \text{if } 0 < X < X_1(t) \\ \dfrac{L-X}{L-X_1(t)} x_1(t) + \dfrac{X - X_1(t)}{L - X_1(t)} L & \text{if } X_1(t) < X < L \end{cases} \tag{7}$$

Differentiating the deformation mapping $\varphi_h(X,t)$ with respect to position X at constant time t, we find the deformation gradient F_h:

$$F_h(X,t) = \begin{cases} \dfrac{x_1(t)}{X_1(t)} & \text{if } 0 < X < X_1(t) \\ \dfrac{L - x_1(t)}{L - X_1(t)} & \text{if } X_1(t) < X < L \end{cases} \tag{8}$$

DOI: 10.1002/nme

In addition, differentiating the deformation mapping $\varphi_h(X,t)$ with respect to time t at constant position X, we find a discretization of the material velocity field $\dot{\varphi}_h$:

$$\dot{\varphi}_h(X,t)=\begin{cases}\dfrac{X}{X_1(t)}\left[\dot{x}_1(t)-\left(\dfrac{x_1(t)}{X_1(t)}\right)\dot{X}_1(t)\right] & \text{if } 0<X<X_1(t)\\ \dfrac{L-X}{L-X_1(t)}\left[\dot{x}_1(t)-\left(\dfrac{L-x_1(t)}{L-X_1(t)}\right)\dot{X}_1(t)\right] & \text{if } X_1(t)<X<L\end{cases} \tag{9}$$

which we refer to as the *consistent velocity field*. Alternatively, the material velocity field can be interpolated independently from the interpolation for the deformation mapping as

$$V_h(X,t)=\begin{cases}\dfrac{X}{X_1(t)}V_1(t) & \text{if } 0<X<X_1(t)\\ \dfrac{L-X}{L-X_1(t)}V_1(t) & \text{if } X_1(t)<X<L\end{cases} \tag{10}$$

where $V_1(t)$ is the velocity of the internal node, assumed *a priori* independent from both $\dot{X}_1$ and $\dot{x}_1$. We remark that if $\dot{X}_1(t)\neq 0$, then the consistent velocity field (9) becomes discontinuous across elements, whereas the *assumed* velocity field (10) remains continuous for every time t.

2.1.2. Standard Galerkin reduction. A set of semi-discrete equations of motion can be obtained by a standard Galerkin reduction of the action, effected by inserting discretizations (7), (8) and (9) into action (2) and rendering the resulting discrete action stationary with respect to $X_1(t)$ and $x_1(t)$. The result is

$$\frac{\mathrm{d}}{\mathrm{d}t}\left\{\mathbb{M}\begin{pmatrix}\dot{X}_1\\ \dot{x}_1\end{pmatrix}\right\}+\frac{R}{6}\begin{pmatrix}-\dfrac{x_1^2}{X_1^2}+\dfrac{(L-x_1)^2}{(L-X_1)^2}\\ 2\left(\dfrac{x_1}{X_1}-\dfrac{L-x_1}{L-X_1}\right)\end{pmatrix}\dot{X}_1^2=\begin{pmatrix}[E]\\ [P]\end{pmatrix} \tag{11}$$

where

$$\mathbb{M}=\frac{RL}{3}\begin{pmatrix}1+\left(\dfrac{L}{X_1}+\dfrac{L}{L-X_1}\right)\left(\dfrac{x_1-X_1}{L}\right)^2 & -1\\ -1 & 1\end{pmatrix} \tag{12}$$

is an extended mass matrix, and $[C]$ and $[F]$ are the jumps in the static Eshelby and Piola–Kirchhoff stress tensors $E(F)=W(F)-PF$ and $P(F)=DW(F)$, respectively. We note that the extended mass matrix is configuration dependent.

The stationarity of the action functional supplies a coupled system of differential equations for the motion of the node in both the reference and the deformed configurations. The first equation of motion governs r-adaption, i.e. the location of the nodes in the reference configuration. It may be regarded as defining *configurational dynamics* for the mesh. The second equation of motion governs the trajectory of the node in the deformed configuration by establishing the classical D'Alembert equilibrium between mechanical and inertia forces.

DOI: 10.1002/nme

2.1.3. Mixed Lagrangian formulation. An alternative set of semi-discrete equations of motion can be obtained by reduction of the *mixed* formulation, effected by inserting discretizations (7), (8) and (10) into the mixed action (5) and rendering the resulting discrete mixed action stationary with respect to $X_1(t)$, $x_1(t)$ as before and, in addition, with respect to $V_1(t)$. The result is

$$\frac{RL}{3}\dot{V}_1 = [E] \tag{13}$$

$$-\frac{RL}{3}\dot{V}_1 = [P] \tag{14}$$

$$V_1 = \dot{x}_1 - \dot{X}_1 \tag{15}$$

or, eliminating V_1,

$$\mathbb{M}\begin{pmatrix} \ddot{X}_1 \\ \ddot{x}_1 \end{pmatrix} = \begin{pmatrix} [E] \\ [P] \end{pmatrix} \tag{16}$$

where

$$\mathbb{M} = \frac{RL}{3}\begin{pmatrix} 1 & -1 \\ -1 & 1 \end{pmatrix} \tag{17}$$

is the mixed extended mass matrix. We note that in this example the extended mass matrix is constant, but this is not the case in general. It should also be carefully noted that the mixed extended mass matrix is singular. However, adding (13) and (14) we obtain the constraint

$$[E] + [P] = 0 \tag{18}$$

to which the trajectory of the system must be confined. It is remarkable that, although in the continuum setting the classical and mixed stationary action principles are equivalent, in the discrete setting they lead to markedly different equations of motion. The behavior of the solutions is also remarkably different, as demonstrated by the following examples.

2.1.4. Comparison of standard and mixed formulations. Figure 1 shows corresponding motions of the one-dimensional body as determined by the standard and mixed equations of motion when the body is released from rest from some initial deformation. For definiteness, in calculations we use the energy density:

$$W(F) = \frac{1}{2}\mu\left(F^2 + \frac{2}{F} - 3\right) \tag{19}$$

Remarkably, although the mixed solution traces a stable cycle, the Galerkin solution goes immediately unstable and the solution breaks down without completing a single cycle. This strikingly different behavior is also clearly apparent in a phase view of the two systems, Figure 2, which concerns the plane (X_1, P_1) with

$$P_1 = \frac{\partial L_h^{\text{mix}}}{\partial \dot{X}_1} = -\frac{RL}{3}V_1 = \frac{RL}{3}(\dot{X}_1 - \dot{x}_1)$$

DOI: 10.1002/nme

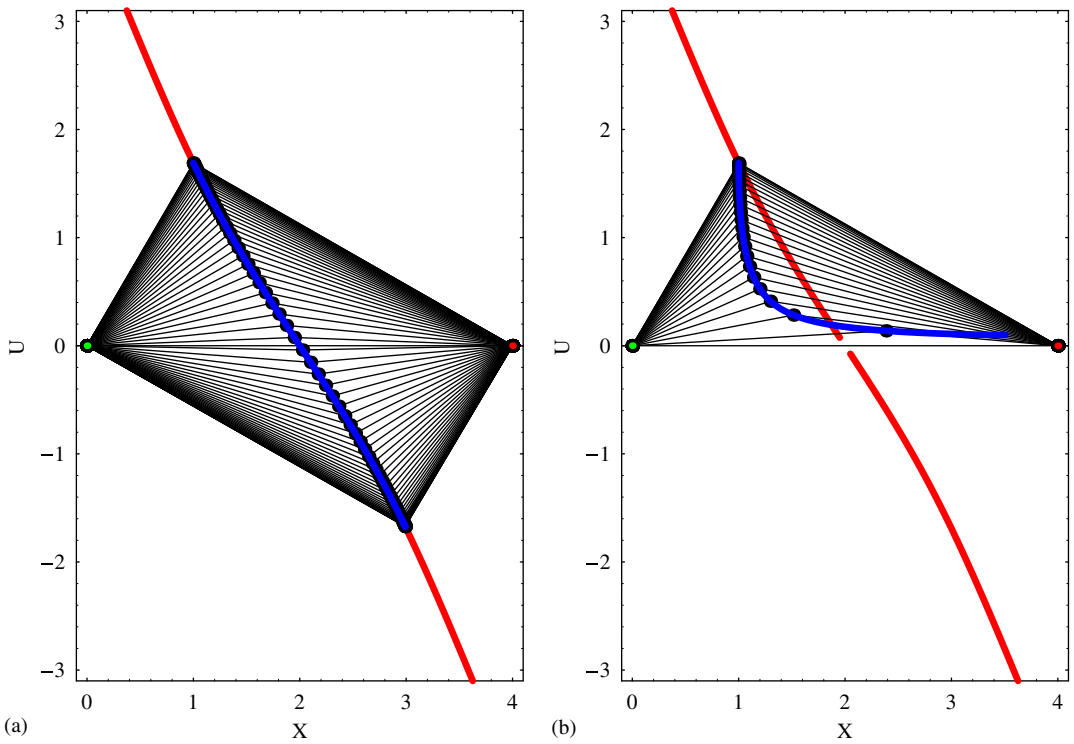

Figure 1. Vibration of a one-dimensional bar discretized into two linear elements. Displacements U as a function of position X at succeeding times: (a) mixed Lagrangian formulation and (b) Galerkin Lagrangian formulation.

for the mixed Lagrangian formulation and

$$P_1 = \frac{\partial L_h}{\partial \dot{X}_1} = \frac{RL}{3}(\dot{X}_1 - \dot{x}_1) + \frac{R}{3}\left(\frac{1}{X_1} + \frac{1}{L - X_1}\right)(x_1 - X_1)\dot{X}_1$$

for the standard Lagrangian formulation. Thus, although the mixed solution traces a closed bounded cycle, the Galerkin solution exhibits clearly unstable behavior.

An additional illustration of this difference in behavior is shown in Figure 3, which collects computed trajectories for bars discretized into an increasing number of elements and set to oscillate by imposing a sinusoidal initial velocity. The energy density in this case is assumed to be of the form:

$$W(F) = \tfrac{3}{2}\mu(F-1)^2 \tag{20}$$

As in the case of the single node released from rest, the mixed formulation returns stable cyclic trajectories of the nodes independently of the initial condition, whereas the Galerkin formulation is catastrophically unstable for almost any initial condition. Remarkably, the final stable location of the nodes in the mixed formulation is not uniform, but approximately sinusoidal, as would

DOI: 10.1002/nme

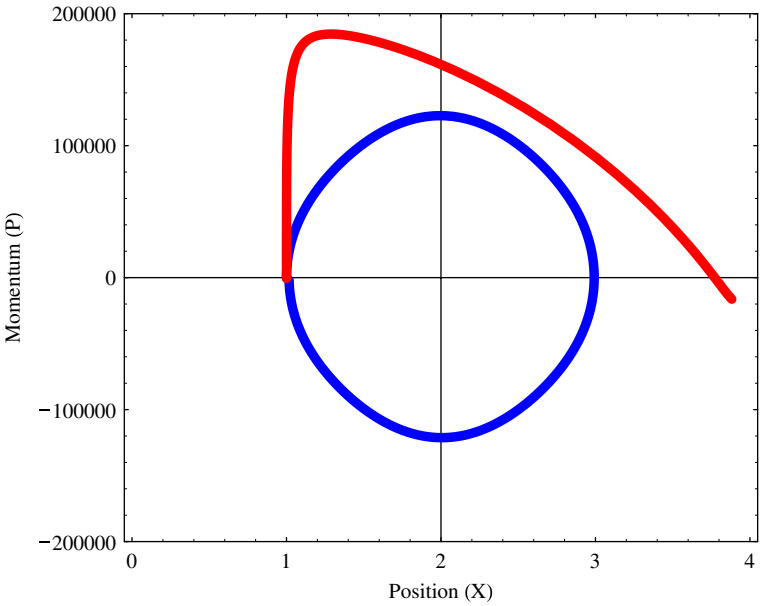

Figure 2. Vibration of a one-dimensional bar discretized into two linear elements. Position–momentum-phase diagram for mixed Lagrangian formulation (stable cycle) and Galerkin Lagrangian formulation (unstable cycle).

be expected from error minimization. The reduction of error resulting from mixed variational r-adaption is further illustrated in Section 6.

2.1.5. Stability analysis. Some preliminary insight into the strikingly unstable behavior of the Galerkin system may be derived from a linearized stability analysis of the equations. Introducing the new variables (U, u) through the relations

$$x_1 = X_1 + uL \tag{21a}$$

$$X_1 = \frac{L}{2} + \varepsilon U L \tag{21b}$$

and expanding the Galerkin equations of motion up to leading order in ε give

$$\frac{RL^2}{3}\begin{pmatrix} 1 & -1 \\ -1 & 1 \end{pmatrix}\begin{pmatrix} \varepsilon\ddot{U} \\ \ddot{u}+\varepsilon\ddot{U} \end{pmatrix} + \frac{4RL^2}{3}\begin{pmatrix} \varepsilon(u^2\ddot{U}+2u\dot{u}\dot{U})-\varepsilon^2 u\dot{U}^2 \\ \varepsilon^2 u\dot{U}^2 \end{pmatrix} = \begin{pmatrix} [E] \\ [P] \end{pmatrix} \tag{22}$$

Projecting these equations on the *tangential direction* $(1, 1)$, i.e. adding both equations, leads to the equation:

$$\frac{4RL^2}{3}(u^2\varepsilon\ddot{U}+2u\dot{u}\varepsilon\dot{U})+[E]+[P]=0 \tag{23}$$

DOI: 10.1002/nme

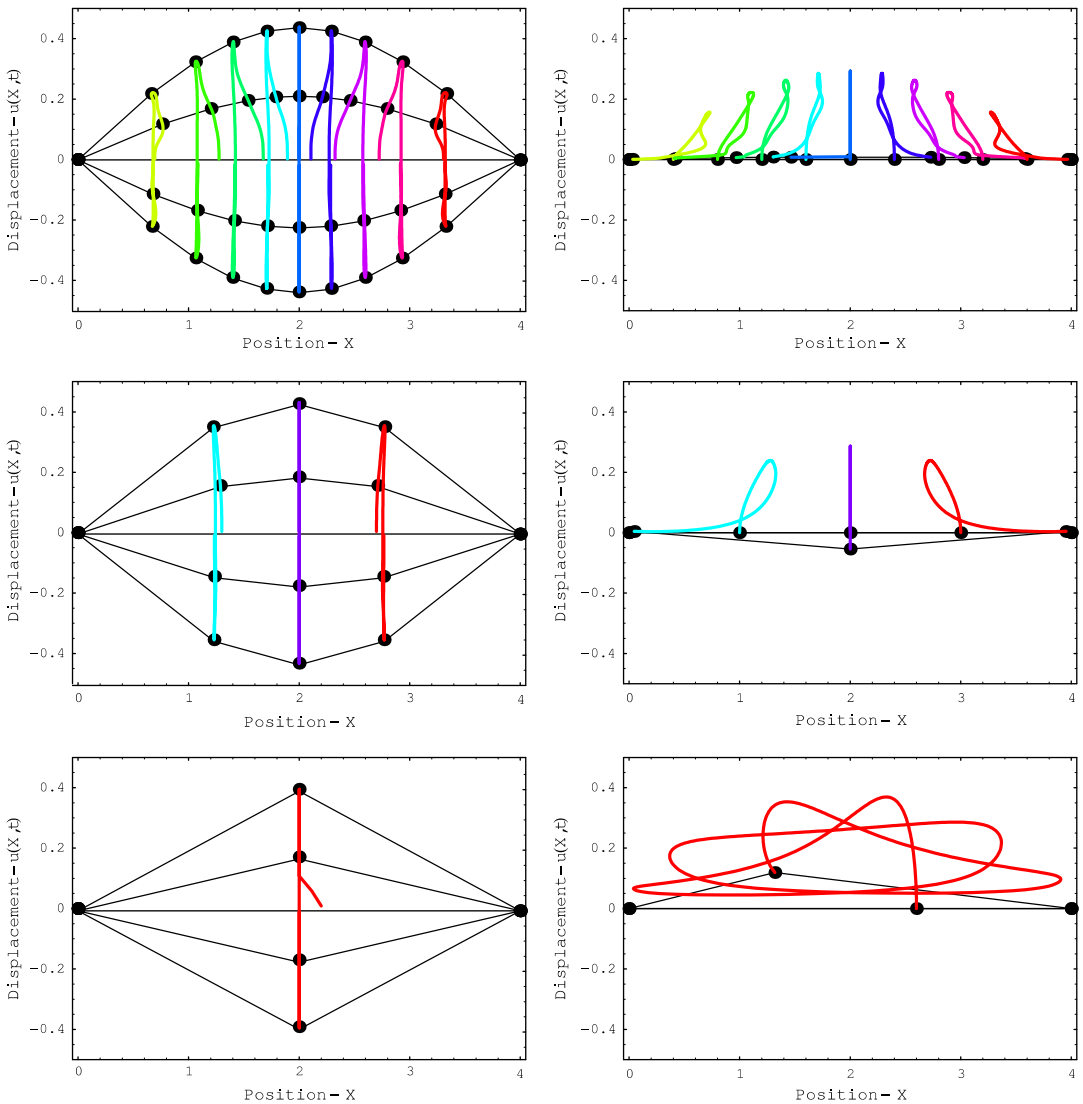

Figure 3. Oscillation of a bar discretized by means of linear elements. Displacements $u(X,t)$ as a function of position at succeeding times for a linear elastic material. Left column: mixed Lagrangian formulation; right column: Galerkin Lagrangian formulations.

which may be contrasted with the corresponding algebraic constraint arising the mixed Lagrangian formulation, namely,

$$[E]+[P]=0 \tag{24}$$

DOI: 10.1002/nme

We note immediately that the term $2u\dot{u}$ in (23), which effectively functions as a non-linear viscosity coefficient, is of undefined sign and, in particular, becomes negative as the system moves toward its undeformed configuration, i.e. when $u\dot{u}<0$, resulting in the observed divergence of the solutions.

3. CLASSICAL AND MIXED HAMILTON'S PRINCIPLES

With the preceding examples by way of motivation and backdrop, we turn to the formulation of a general mixed, or two-field, variational principle for dynamics that allows for independent variations of deformations φ and velocities V. We will refer to this principle as the *mixed Hamilton's principle*. The construction of this mixed variational principle follows a standard—Lagrange multiplier argument to enforce the *time-compatibility* identity $V=\dot{\varphi}$ between the *assumed* V and *compatible* $\dot{\varphi}$ velocity fields. In the subsequent section we extend this formulation to account for variations with respect to defect rearrangements or *horizontal variations*. The resulting mixed three-field formulation simultaneously delivers the equations of balance of mechanical forces, configurational forces and time compatibility.

The mixed formulation for dynamics is introduced as an approach to overcome instabilities inherent to the use of the standard or *single-field* Hamilton's principle with moving meshes. More specifically, as illustrated by the examples in the previous section, the consistent discretized velocity field $\dot{\varphi}_h$ is discontinuous across element boundaries, in general when the nodes are allowed to move in the reference configuration. These discontinuities may grow unstably and the approximation scheme breaks down. These instabilities are effectively controlled by making use of a conforming, i.e. continuous, assumed velocity interpolation V_h in lieu of the consistent interpolation $\dot{\varphi}_h$ and by adopting the mixed Hamilton's principle as the underlying variational framework.

The mixed variational formulation presented here may be considered as a temporal analog of the de Veubeke–Hu–Washizu mixed variational principle for statics (cf., e.g. [25, 26]). Furthermore, both variational principles may be combined together to establish a single mixed space–time variational principle for non-linear dynamics that accounts for independent variations of all fields, namely, displacements, deformations, velocities, stresses and momenta. However, this degree of generality will not be pursued in this paper in the interest of simplicity.

3.1. Classical Hamilton's principle

We recall by way of background that the classical action functional of elastodynamics is

$$S[\varphi]=\int_{t_0}^{t_f}\left\{\int_B L(X,t,\varphi,\dot{\varphi},\nabla\varphi)\,\mathrm{d}V+\int_{\partial B_1}\bar{T}\cdot\varphi\,\mathrm{d}S\right\}\mathrm{d}t \tag{25}$$

where $B\subset\mathbb{R}^3$ is the reference or undeformed configuration of the body; ∂B is the boundary of B; $\partial B_1\subset\partial B$ is the Neumann or traction boundary; $\varphi: B\times(t_0,t_f)\to\mathbb{R}^3$ is the deformation mapping; $\bar{T}:\partial B_1\times(t_0,t_f)\to\mathbb{R}^3$ are the applied tractions; and $L(X,t,\varphi,\dot{\varphi},\nabla\varphi)$ is the Lagrangian density per unit undeformed volume. The deformation mapping is subject to essential boundary conditions:

$$\varphi(X,t)=\bar{\varphi}(X,t),\quad X\in\partial B_0 \tag{26}$$

over the Dirichlet or displacement boundary $\partial B_0=\partial B\backslash\partial B_1$, where $\bar{\varphi}(X,t)$ is the prescribed deformation mapping. The trajectories of the system having fixed initial and final conditions,

DOI: 10.1002/nme

i.e. such that

$$\varphi(X, t_0) = \varphi_0(X) \tag{27a}$$

$$\varphi(X, t_f) = \varphi_f(X) \tag{27b}$$

follow from Hamilton's principle of stationary action

$$\delta S = 0 \tag{28}$$

where, in accordance with (27), the variations of φ must satisfy homogeneous initial and final conditions:

$$\delta\varphi(X, t_0) = 0 \tag{29a}$$

$$\delta\varphi(X, t_f) = 0 \tag{29b}$$

A standard derivation then gives the corresponding Euler–Lagrange equations as

$$\partial_\varphi L - \nabla\cdot\partial_{\nabla\varphi} L - \frac{\mathrm{d}}{\mathrm{d}t}\partial_{\dot\varphi} L = 0 \quad \text{in } B\times(t_0, t_f) \tag{30a}$$

$$\partial_F L N + \bar{T} = 0 \quad \text{on } \partial B_1\times(t_0, t_f) \tag{30b}$$

A specific class of Lagrangian densities that we consider in calculations is

$$L(X, t, \varphi, \dot\varphi, \nabla\varphi) = \tfrac{1}{2} R(X)|\dot\varphi|^2 - U(X, t, \varphi, \nabla\varphi) \tag{31}$$

where $R(X)$ is the material mass density per unit undeformed volume, and $U(X, t, \varphi, \nabla\varphi)$ is the potential energy density per undeformed volume. In the case of body forces of the dead-load type, $U(X, t, \varphi, \nabla\varphi)$ further reduces to the form:

$$U(X, t, \varphi, \nabla\varphi) = W(X, \nabla\varphi) - B(X, t)\cdot\varphi \tag{32}$$

where $W(X, \nabla\varphi)$ is the strain-energy density per unit undeformed volume and $B(X, t)$ the body force density per unit undeformed volume. This class of Lagrangians suffices to describe the standard case of an inhomogeneous elastic material undergoing finite deformations under the action of applied body forces and tractions. For Lagrangians of form (31), the classical equations of motion reduce to the familiar form:

$$B + \nabla\cdot\partial_{\nabla\varphi} W - R\ddot\varphi = 0 \quad \text{in } B\times(t_0, t_f) \tag{33a}$$

$$-\partial_{\nabla\varphi} W N + \bar{T} = 0 \quad \text{on } \partial B_1\times(t_0, t_f) \tag{33b}$$

where we recognize the classical equations of motion of elastodynamics and the traction boundary conditions, respectively. In these equations, $\ddot\varphi$ is the acceleration field and $\partial_{\nabla\varphi} W$ is the Piola–Kirchhoff stress tensor.

DOI: 10.1002/nme

3.2. Mixed Hamilton's principle

In the classical action (25), the velocity field $\dot{\varphi}$ follows *strongly* from the deformation mapping φ by pointwise differentiation in time. Motivated by the example of Section 2, instead we wish the velocity field to be an independent field bearing a weak relation to the deformation mapping. To this end, proceeding according to the HP principle and by analogy with the de Veubeke–Hu–Washizu principle, we consider the following three-field *mixed action functional* for elastodynamics:

$$S^{\text{mix}}[\varphi, V, P] = \int_{t_0}^{t_f} \left\{ \int_B [L(X, t, \varphi, V, \nabla\varphi) + P \cdot (\dot{\varphi} - V)] \, \mathrm{d}V + \int_{\partial B_1} \bar{T} \cdot \varphi \, \mathrm{d}S \right\} \mathrm{d}t \tag{34}$$

where $V : B \times (t_0, t_f) \to \mathbb{R}^3$ is the material velocity field; $P : B \times (t_0, t_f) \to \mathbb{R}^3$ is the material linear momentum density per unit undeformed volume; and $L(X, t, \varphi, V, \nabla\varphi)$ is the Lagrangian density per unit undeformed volume. The material momentum density P may be regarded as the Lagrange multiplier that enforces weakly the *time-compatibility* condition $\dot{\varphi} = V$. As in the classical setting, the trajectories of the system satisfying the initial and final conditions (27) follow by enforcing the stationarity of the mixed action (34). Assuming sufficient regularity, a straightforward derivation then gives the corresponding Euler–Lagrange equations as

$$\partial_\varphi L - \nabla \cdot \partial_{\nabla\varphi} L - \dot{P} = 0 \quad \text{in } B \times (t_0, t_f) \tag{35a}$$

$$\partial_V L - P = 0 \quad \text{in } B \times (t_0, t_f) \tag{35b}$$

$$\dot{\varphi} - V = 0 \quad \text{in } B \times (t_0, t_f) \tag{35c}$$

$$\partial_{\nabla\varphi} L + \bar{T} = 0 \quad \text{on } \partial B_1 \times (t_0, t_f) \tag{35d}$$

which correspond to the mechanical equations of motion, time compatibility and traction boundary conditions, respectively.

The preceding three-field formulation can be reduced to a simpler two-field formulation by enforcing identity (35b) pointwise, resulting in the reduced action:

$$S^{\text{mix}}[\varphi, V] = \int_{t_0}^{t_f} \left\{ \int_B L^{\text{mix}}(X, t, \varphi, \dot{\varphi}, V, \nabla\varphi) \, \mathrm{d}V + \int_{\partial B_1} \bar{T} \cdot \varphi \, \mathrm{d}S \right\} \mathrm{d}t \tag{36}$$

where

$$L^{\text{mix}}(X, t, \varphi, \dot{\varphi}, V, \nabla\varphi) \equiv L(X, t, \varphi, V, \nabla\varphi) + \frac{\partial L}{\partial V} \cdot (\dot{\varphi} - V) \tag{37}$$

which we regard as a *mixed* Lagrangian density. The corresponding Euler–Lagrange equations now follow as

$$\partial_\varphi [L + \partial_V L(\dot{\varphi} - V)] - \nabla \cdot \partial_{\nabla\varphi} [L + \partial_V L(\dot{\varphi} - V)] - \frac{\mathrm{d}}{\mathrm{d}t} \partial_V L = 0 \tag{38a}$$

$$\partial_V \partial_V L(\dot{\varphi} - V) = 0 \tag{38b}$$

$$\nabla \cdot \partial_{\nabla\varphi} [L + \partial_V L(\dot{\varphi} - V)] N + \bar{T}_i = 0 \tag{38c}$$

DOI: 10.1002/nme

We verify that these Euler–Lagrange equations are indeed equivalent to (30). For Lagrangian densities of form (31), the Euler–Lagrange equations reduce to

$$B+\nabla\cdot\partial_{\nabla\varphi}W-R\dot{V}=0 \tag{39a}$$

$$R(\dot{\varphi}-V)=0 \tag{39b}$$

$$-[\partial_{\nabla\varphi}W]N+\bar{T}=0 \tag{39c}$$

which are also equivalent to (33).

3.3. Configurational force balance

In analogy to the single-field Hamilton's principle, the mixed Hamilton's principle can be generalized in a way leading to a statement of balance of dynamical configurational forces. To this end, we introduce a *reference manifold* M whose points are identified with objects that move with respect to material particles (Figure 4). These include material defects such as dislocations and vacancies, and, in the case of r-adaption, the nodes of the finite element mesh. In addition, we introduce an embedding $\Psi: M\times(t_0,t_f)\to B\subset\mathbb{R}^3$ describing the arrangement of defects in the reference or material configuration B, and an embedding $\psi: M\times(t_0,t_f)\to\mathbb{R}^3$ describing the placement of defects in the deformed or spatial configuration; and the *deformation mapping*

$$\varphi=\psi\circ\Psi^{-1}: B\to\mathbb{R}^3 \tag{40}$$

The points of B are identified with the *material particles*. Finally, we introduce the defect velocity field $v=V\circ\Psi: M\to\mathbb{R}^3$. The mappings Ψ and ψ are sometimes referred to as the *horizontal* and *vertical* motions of the body (see [17–19, 27]). The identification of deformable bodies as embedded manifolds, with a careful differentiation between coordinate systems, material particles and the region of space occupied by the body, is one of the standard formalisms of continuum mechanics [28]. Truesdell and Noll attribute their introduction to Lodge [29]. This distinction also supplies a framework for the definition of configurational forces (see, e.g. [18, 30]).

Inserting representation (40) into the mixed action (36) gives

$$S[\Psi,\psi,v]=\int_{t_0}^{t_f}\int_M\{L(\Psi,t,\psi,v,\nabla\psi\nabla\Psi^{-1})+Rv[\dot{\psi}-(\nabla\psi\nabla\Psi^{-1})\dot{\Psi}-v]\}\det(\nabla\Psi)\,\mathrm{d}\xi\,\mathrm{d}t \tag{41}$$

where we have assumed $\partial_1=\emptyset$ for simplicity and we have made use of the identity

$$\dot{\varphi}\circ\Psi=\dot{\psi}-(\nabla\psi\nabla\Psi^{-1})\dot{\Psi} \tag{42}$$

We now regard action (41) as an independent functional of the horizontal motion Ψ, the vertical motion ψ and the particle velocity field v. Assuming sufficient regularity, the stationarity of (41) with respect to each of its arguments gives the Euler–Lagrange equations

$$B+\nabla\cdot\partial_{\nabla\varphi}W-R\dot{V}=0 \tag{43a}$$

$$C+\nabla\cdot E-R\frac{\mathrm{d}}{\mathrm{d}t}(-F^{\mathrm{T}}V)-R\nabla[V\cdot(\dot{\varphi}-V)]=0 \tag{43b}$$

$$R(\dot{\varphi}-V)=0 \tag{43c}$$

DOI: 10.1002/nme

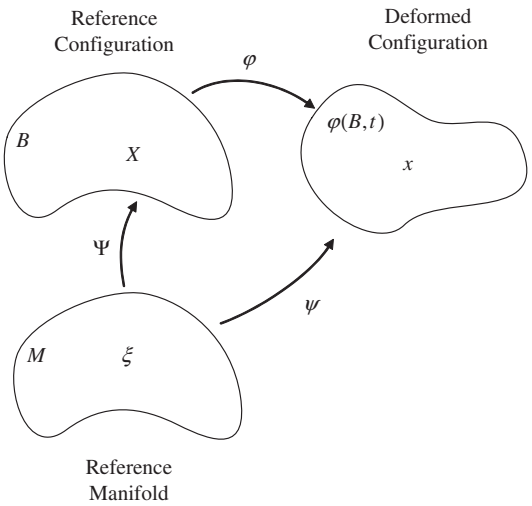

Figure 4. Reference manifold, reference configuration, deformed configuration and related embedding.

where we have restricted the attention to Lagrangians of the form (31); for simplicity,

$$C = \partial_X L|_{\exp} = \tfrac{1}{2}\partial_X R\,|V|^2 - \partial_X W|_{\exp} \tag{44}$$

is the inhomogeneity force field and

$$E = -(LI - F^{\mathrm{T}}\partial_{\nabla\varphi} L) = (W - \tfrac{1}{2}R|V|^2)I - F^{\mathrm{T}}\partial_{\nabla\varphi} W \tag{45}$$

is the dynamical Eshelby energy–momentum tensor field (see [5, 6]). In (44) the label exp denotes the derivative with respect to the explicit dependence on X.

In (43a) and (43b) we recognize the vertical Euler–Lagrange equations of the mixed action. If the body is homogeneous and free of defects, a straightforward differentiation shows that the field equation (43b) is automatically satisfied as a consequence of (43a) and (43c). Otherwise, Equation (43b) furnishes an additional field equation that governs the dynamic rearrangement of defects and homogeneities in the body.

We note that the approach we have followed above for the definition of configurational forces is the so-called 'variational approach'. Alternative formulations are (i) the 'pull-back' approach [31–34], in which configurational force balance is regarded as the projection (pull-back) of the mechanical force balance equations onto the material manifold and configurational forces are related to the concept of *material uniformity and homogeneity* [28, 35] as the forces behind *continuous distribution of inhomogeneities* (see [36–40]); (ii) the *basic primitive objects* approach of Gurtin (see [41–44]), where configurational forces are postulated as primitive physical entities, independent of mechanical forces, and their balance is derived using invariance arguments; (iii) Noether's theorem approach (see [17, 19, 34, 45–47]), where conservation (alternatively, lack of conservation) of configurational forces arises as the conservation law associated with material translational symmetry (alternatively, lack of symmetry) of the Lagrangian density; and (iv) the *inverse motion* approach (see [31, 48–50]) for which the equations of balance of configurational

DOI: 10.1002/nme

forces follow from the stationarity of the energy or action functional with respect to the reference configuration keeping the current configuration fixed.

3.4. Geometrical interpretation

The variational approach just outlined admits the following useful geometrical interpretation. Consider the *space–space* bundle, i.e. the set $E = B \times S$ where $S = \mathbb{R}^n$ is the ambient space, Figure 5. Local coordinates for any point in this bundle are (X, x) and its projection map is $\pi : E \to B$ given in coordinates by $\pi(X, x) = X$. For a fixed time t, consider the graph $f_t(X) = (X, \varphi(X, t))$ of the deformation mapping φ at time t. This graph is an n-dimensional manifold immersed in an $2n$-dimensional space, the space–space bundle $B \times S$, and is one of its sections, i.e. $\pi \circ f_t = Id : B \to B$, the identity map in B. This situation is shown graphically in Figure 5, where the horizontal axis represents the material manifold B and the vertical axis the space S. The graph $f_t(X)$ for a given time t can be then represented as a curve in $B \times S$ with X acting as a parameter.

We note now that $f_t(X) = (X, \varphi(X, t))$ is only one particular parametrization of the graph manifold at time t, i.e. a parametrization with parameter X. Consider any alternative parametrization $g_t(\xi) = (\Psi(\xi, t), \psi(\xi, t))$ of the *same* manifold, where $\xi \in M$ is a new parameter and M is a new parameter set. For $f_t(X)$ and $g_t(\xi)$ to be two different parametrizations of the *same* graph, the component functions must be related by

$$\varphi(\Psi(\xi, t), t) = \psi(\xi, t) \tag{46}$$

which is nothing else but Equation (40). It follows that the *reference manifold M* can be reinterpreted as a reparametrization of the base space B and that the mappings $(\Psi(\xi, t), \psi(\xi, t))$ are, respectively, the *horizontal* and *vertical* coordinates of any point on the graph manifold parametrized with the new parameter ξ. Furthermore, a variation $(0, \delta\psi)$ can be interpreted as a vertical perturbation of the graph manifold or *vertical variation* and a variation $(\delta\Psi, 0)$ as an horizontal perturbation or *horizontal variation*.

4. SPATIAL DISCRETIZATION

The classical and mixed Lagrangians introduced in the foregoing sections call for two different types of discretizations of the velocity field. In the case of the classical Lagrangian, the velocity field is computed by direct differentiation with respect to time of the deformation mapping, whereas in the case of the mixed Lagrangian, the velocity field can be interpolated independently of the deformation mapping. In this section we briefly describe these two types of interpolations and the structure of the resulting semi-discrete equations of motion.

We consider a time-dependent family of triangulations $\mathscr{T}_h(t)$ of the reference configuration B. For simplicity, we confine attention to the case in which the node set of $\mathscr{T}_h(t)$ is allowed to move continuously in time within the reference configuration while the mesh topology, i.e. the connectivity and number of nodes and elements, remains unchanged. We additionally consider finite element interpolations of the deformation mapping $\varphi(X, t)$ of the form:

$$\varphi_h(X, t) = \sum_{a=1}^{N} N_a(X, t) x_a(t) = \sum_{e}^{E} \sum_{a=1}^{n} N_a^e(X, t) x_a^e(t) \tag{47}$$

DOI: 10.1002/nme

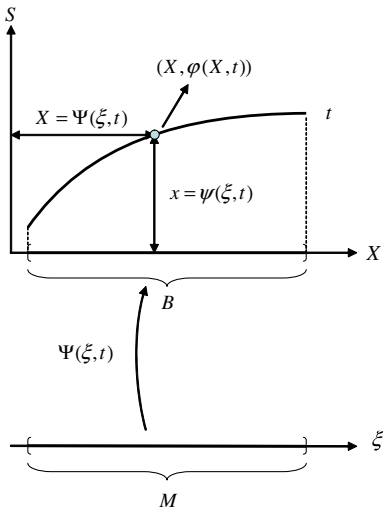

Figure 5. Graph of the deformation mapping as a manifold (section) of the space–space bundle.

where N is the total number of nodes; E is the total number of elements; n is the total number of nodes per element; $N_a(X,t)$ is the global shape function for node a at time t; $N_a^e(X,t)$ is the local shape function for node a and element e at time t, extended to be zero outside element e; $x_a(t)$ are the spatial coordinates of the node in the deformed configuration at time t; and $x_a^e(t)$ are the spatial coordinates of node a of element e at time t. It should be carefully noted that the shape functions $N_a(X,t)$ are time dependent in general due to the motion of the nodes in the reference configuration.

We restrict attention throughout to isoparametric finite element interpolation. In particular, we introduce the time-dependent horizontal and vertical isoparametric mappings:

$$\Psi_h(\xi,t) = \sum_e^E \sum_{a=1}^n \hat{N}_a(\xi) X_a^e(t) \tag{48a}$$

$$\psi_h(\xi,t) = \sum_e^E \sum_{a=1}^n \hat{N}_a(\xi) x_a^e(t) \tag{48b}$$

mapping the standard element domain $\hat{\Omega}$ to the material and spatial domains of element e at time t, respectively (Figure 6). In this expression $\hat{N}_a$ are the standard shape functions over $\hat{\Omega}$. Then, the isoparametric shape functions are $N_a^e = \hat{N}_a \circ \Psi^{e-1}$, or, explicitly,

$$N_a^e(X,t) = \hat{N}_a(\Psi^{e-1}(X,t)) \tag{49}$$

and the deformation mapping admits the representation

$$\varphi_h = \psi_h \circ \Psi_h^{-1} \tag{50}$$

which should be carefully contrasted with representation (40). We emphasize that the nodal coordinates in the *reference* configuration X_a are assumed to be time dependent and regarded as *unknowns*

DOI: 10.1002/nme

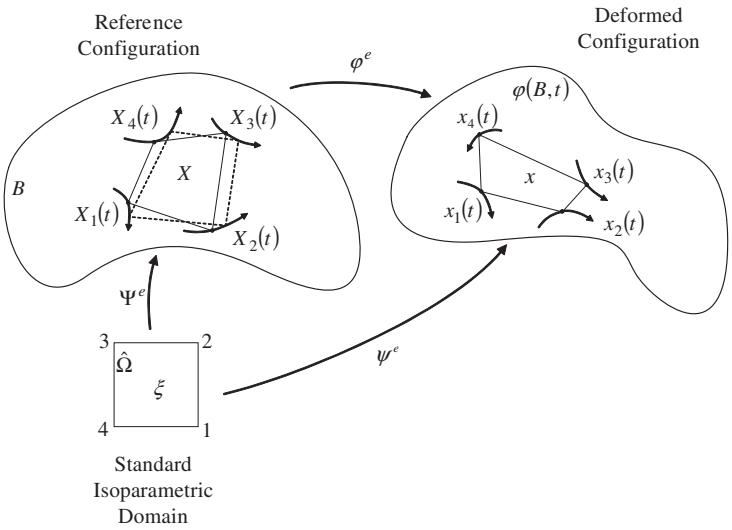

Figure 6. An isoparametric *moving* element and related mappings. Note that nodes are assumed to move continuously in time within the reference configuration, simultaneously with the motion of the body.

to be solved jointly with the nodal spatial motion $x_a(t)$. This results in an isoparametric *moving* element that migrates continuously in time within the reference configuration, simultaneously with the body motion. This situation is depicted in Figure 6.

One key virtue of the isoparametric representation is to reduce time-dependent interpolations to time-independent interpolations over the standard domain, which greatly facilitates taking proper rates of time-dependent fields. This aspect of the isoparametric representation is particularly useful when dealing with time-dependent interpolations, such as those considered here. Another benefit of adopting the isoparametric representation is that, by virtue of identity (50), the mappings Ψ_h and ψ_h may naturally be regarded as discrete horizontal and vertical motions in the sense discussed in Section 3.3 and used as a basis for defining a discrete configurational force system.

Next we consider the consistent material velocity field $\dot{\varphi}_h$. Differentiating the discretized deformation mapping (47) gives, after the straightforward calculation in the Appendix,

$$\dot{\varphi}_h(X,t)=\sum_{e}^{E}\sum_{a=1}^{n} N_a^e(\dot{x}_a^e - F^e\dot{X}_a^e) \tag{51}$$

where

$$F_{iI}^e(X,t)=(\nabla\varphi_h^e)_{iI}(X,t)=\sum_{a=1}^{n} x_{ai}^e(t)\frac{\partial N_a^e}{\partial X_I}(X,t) \tag{52}$$

is the local deformation gradient field. It should be carefully noted that the consistent velocity $\dot{\varphi}_h$ exhibits jumps across element boundaries resulting from its dependence on the discretized deformation gradient $\nabla\varphi_h$, which is also discontinuous across elements.

As illustrated by the examples in Section 2, the jumps of the consistent velocity field (51) across elements may grow unbounded as a result of numerical instabilities, whereupon the approximation

DOI: 10.1002/nme

scheme breaks down. In order to sidestep this difficulty, within the framework of the mixed-Lagrangian formulation (36), (37), we introduce an *independent* finite element interpolation of the velocity field of the form:

$$V_h(X,t)=\sum_{a=1}^{N} N_a(X,t)V_a(t)=\sum_{e}^{E}\sum_{a=1}^{n} N_a^e(X,t)V_a^e(t) \tag{53}$$

where $V_a(t)$ is the velocity of node a at time t, and $V_a^e(t)$ is the velocity of node a of element e at time t. It bears emphasis that the discretized deformation mapping and velocity field are interpolated by conforming shape functions and that, in particular, the discretized velocity field remains continuous at all times.

A semi-discrete mixed action functional may now be defined by restricting the continuous mixed action functional (36) to deformation mappings and velocity fields of form (47) and (53), respectively, with the result

$$S_h^{\mathrm{mix}}[X_h, x_h, V_h]=\int_{t_0}^{t_f} L_h^{\mathrm{mix}}(X_h(t), x_h(t), \dot{X}_h(t), \dot{x}_h(t), V_h(t))\,\mathrm{d}t \tag{54}$$

where $x_h(t)=\{x_a(t), a=1,\ldots,N\}$, $X_h(t)=\{X_a(t), a=1,\ldots,N\}$ and $V_h(t)=\{V_a(t), a=1,\ldots,N\}$ are the global arrays of nodal coordinates in the reference and deformed configurations and nodal velocities, respectively, and L_h is a semi-discrete mixed Lagrangians given by

$$L_h^{\mathrm{mix}}(X_h, x_h, \dot{X}_h, \dot{x}_h, V_h)=\sum_{e}^{E}\int_{\Omega^e(X_h^e)} L^{\mathrm{mix}}(X, t, \varphi_h^e, \dot{\varphi}_h^e, V_h^e, \nabla\varphi_h^e)\,\mathrm{d}V \tag{55}$$

where $L^{\mathrm{mix}}(X,t,\varphi,\dot{\varphi},V,\nabla\varphi)$ is the mixed Lagrangian density (37). For a Lagrangian density of the form (31), the local semi-discrete mixed Lagrangian takes the form

$$L_h^{\mathrm{mix}}=\tfrac{1}{2}V_h^{\mathrm{T}}m_h(X_h)V_h-I_h(t,X_h,x_h)+V_h^{\mathrm{T}}(m_h(X_h)\dot{x}_h+M_h(X_h,x_h)\dot{X}_h-m_h(X_h)V_h) \tag{56}$$

where the horizontal and vertical mass matrices M_h and m_h are assembled from element contributions as

$$M_{aibJ}(X_h,x_h)=-\sum_{e=1}^{E}\int_{\Omega^e(X_h^e)} RF_{iJ}^e N_a^e N_b^e\,\mathrm{d}V \tag{57a}$$

$$m_{aibj}(X_h)=\sum_{e=1}^{E}\int_{\Omega^e(X_h^e)} R\delta_{ij}N_a^e N_b^e\,\mathrm{d}V \tag{57b}$$

respectively, and

$$I_h(t,X_h,x_h)=\sum_{e=1}^{E}\left\{\int_{\Omega^e(X_h^e)}[W(X,\nabla\varphi_h^e)-B(X,t)\cdot\varphi_h^e]\,\mathrm{d}V-\int_{\Omega^e(X_h^e)\cap\partial B_1}\bar{T}_h\cdot\varphi_h^e\,\mathrm{d}S\right\} \tag{58}$$

is the discretized potential energy. Taking variations of the semi-discrete action functional and enforcing stationarity, a lengthy but straightforward calculation gives the Euler–Lagrange equations:

$$\frac{\mathrm{d}}{\mathrm{d}t}(m_h^{\mathrm{T}}V_h)=f_h \tag{59a}$$

DOI: 10.1002/nme

$$\frac{\mathrm{d}}{\mathrm{d}t}(M_h^{\mathrm{T}} V_h) = F_h \tag{59b}$$

$$m_h \dot{x}_h + M_h \dot{X}_h = m_h V_h \tag{59c}$$

where

$$F_a = \sum_{e=1}^{E} \left\{ \int_{\Omega^e(X_h^e)} (C_h^{e-\text{static}} N_a^e - E_h^{e-\text{static}} \nabla N_a^e)\,\mathrm{d}V + \int_{\Omega^e(X_h^e)} R(F_h^{e\mathrm{T}} V_h^e)(\nabla N_a^e \cdot \dot{X}_h^e)\,\mathrm{d}V \right.$$
$$\left. + \int_{\Omega^e(X_h^e)} \nabla(R N_a^e) \left(\frac{1}{2} |V_h^e|^2 + V_h^e \cdot (\dot{x}_h^e - \nabla \varphi_h^e \dot{X}_h^e - V_h^e) \right) \mathrm{d}V \right\} \tag{60a}$$

$$f_a = \sum_{e=1}^{E} \left\{ \int_{\Omega^e(X_h^e)} (B_h^e N_a^e - \partial_{\nabla\varphi} W_h^e \nabla N_a^e)\,\mathrm{d}V - \int_{\Omega^e(X_h^e)} R V_h^e (\nabla N_a^e \cdot \dot{X}_h^e)\,\mathrm{d}V \right\} \tag{60b}$$

are the nodal configurational and mechanical forces, respectively; $C_h^{e\text{-static}}$ and $E_h^{e\text{-static}}$ are the *static* inhomogeneity force and *static* Eshelby stress tensor, i.e. those derived from the energy density W instead of the Lagrangian density L; B_h^e is the local body-force field and $\partial_{\nabla\varphi} W_h^e$ is the local Piola–Kirchhoff tensor field, and we express

$$\dot{X}_h^e = \sum_{a=1}^{n} \dot{X}_a^e N_a^e \tag{61a}$$

$$\dot{x}_h^e = \sum_{a=1}^{n} \dot{x}_a^e N_a^e \tag{61b}$$

In Equations (59a) we recognize the discrete counterpart of the Euler–Lagrange Equations (43a).

5. TIME DISCRETIZATION

The final step in the discretization of the mixed action (36) is to effect a time discretization of the corresponding semi-discrete action (54). It is, of course, possible to discretize the semi-discrete Euler–Lagrange equations directly by means of a conventional time-stepping algorithm such as Newmark's. However, Newmark's algorithm family is not well suited to the systems with configuration-dependent mass matrices of interest here. In addition, *variational integrators* (see, for instance, [18, 19] for a review), in which the semi-discrete action is discretized in time directly, have been shown to possess superior conservation and accuracy properties than conventional time-stepping algorithms and therefore immediately suggest themselves. We begin by collecting all dynamical variables into the generalized coordinate array $q_h = (X_h, x_h)$ in order to streamline the notation. Next, we partition the time interval $[t_0, t_f]$ into discrete times $(t_0, \ldots, t_k, \ldots, t_K = t_f)$ where K is the number of time steps. On the basis of this time partition, we interpolate the trajectories $q_h(t)$ and velocities $V_h(t)$ by means of piecewise linear functions of time and piecewise

DOI: 10.1002/nme

constant functions, respectively, i.e

$$q_h(t) = q_k\left(\frac{t_{k+1}-t}{t_{k+1}-t_k}\right)+q_{k+1}\left(\frac{t-t_k}{t_{k+1}-t_k}\right), \quad t\in[t_k,t_{k+1}] \tag{62a}$$

$$V_h(t) = V_{k+\alpha}, \quad t\in[t_k,t_{k+1}] \tag{62b}$$

where $V_{k+\alpha}$ is constant in the interval (t_k,t_{k+1}). This choice of interpolation is natural from the standpoint of mixed methods, since it places the space of deformation mapping histories, modulo time shifts and the space of velocity histories in one-to-one correspondence. Inserting interpolation (62a) into the semi-discrete action (54) and evaluating all integrals by the trapezoidal rule give the fully discrete action:

$$S_d^{\mathrm{mix}}(\ldots,t_k,q_k,V_h^{k+\alpha},\ldots)=\sum_{k=0}^{K} L_d^{\mathrm{mix}}(t_k,t_{k+1},q_k,q_{k+1},V_h^{k+\alpha}) \tag{63}$$

where

$$\begin{aligned} &L_d^{\mathrm{mix}}(t_k,t_{k+1},q_k,q_{k+1},V_{k+\alpha})\\ &\quad=(t_{k+1}-t_k)\left[\frac{1}{2}V_{k+\alpha}^{\mathrm{T}}m_{k+\alpha}V_{k+\alpha}-\frac{1}{2}(I_{k+\alpha}+I_{k+1-\alpha})\right]\\ &\qquad+(t_{k+1}-t_k)\left[V_{k+\alpha}^{\mathrm{T}}m_{k+\alpha}\left(m_{k+\alpha}^{-1}(M_{k+\alpha},m_{k+\alpha})\frac{q_{k+1}-q_k}{t_{k+1}-t_k}-V_{k+\alpha}\right)\right] \end{aligned} \tag{64}$$

is the discrete action. The discrete trajectories are now obtained by rendering the discrete action stationary, i.e. from the discrete mixed Hamilton principle

$$\delta S_d^{\mathrm{mix}}=0 \tag{65}$$

The discrete Euler–Lagrange equations corresponding to this principle take the form

$$\partial_{q_k}L_d^{\mathrm{mix}}(t_k,t_{k+1},q_k,q_{k+1},V_{k+\alpha})+\partial_{q_k}L_d^{\mathrm{mix}}(t_{k-1},t_k,q_{k-1},q_k,V_{k-1+\alpha})=0 \tag{66a}$$

$$\partial_{V_{k+\alpha}}L_d^{\mathrm{mix}}(t_k,t_{k+1},q_k,q_{k+1},V_{k+\alpha})=0 \tag{66b}$$

which constitutes a coupled system of three equations for the determination of the update of the referential nodal coordinates, spatial nodal coordinates and velocity $q_{k+1},V_{k+\alpha}$ in terms of the current configuration q_k and velocity $V_{k-1+\alpha}$. Taking variations with respect to t_k yields an additional discrete energy-balance equation, which, when solvable, can be used to determine optimal time steps [51]. However, this extension of the method will not be pursued here in the interest of simplicity. The discrete Euler–Lagrange equations evaluate to

$$M_{k+\alpha}V_{k+\alpha}-M_{k-1+\alpha}V_{k-1+\alpha}=(1-\alpha)(t_{k+1}-t_k)F_{k+\alpha}+\alpha(t_k-t_{k-1})F_{k-1+\alpha} \tag{67a}$$

$$m_{k+\alpha}V_{k+\alpha}-m_{k-1+\alpha}V_{k-1+\alpha}=(1-\alpha)(t_{k+1}-t_k)f_{k+\alpha}+\alpha(t_k-t_{k-1})f_{k-1+\alpha} \tag{67b}$$

$$(M_{k+\alpha},m_{k+\alpha})\frac{q_{k+1}-q_k}{t_{k+1}-t_k}-m_{k+\alpha}V_{k+\alpha}=0 \tag{67c}$$

DOI: 10.1002/nme

6. NUMERICAL TESTS

In this section we present a suite of tests and examples designed to assess the performance of the methodology developed in the foregoing. The first example is designed to measure the accuracy of the method and concerns a problem involving gas dynamics in a shock tube configuration for which the exact analytical solution can be obtained in closed form. This problem has been used as a benchmark to study the convergence and accuracy of other mesh adaption strategies (cf. [1]). The second example involves a block of non-linear elastic material subjected to the application of a moving point load. The third and last example concerns the propagation of a crack along a predetermined crack path.

6.1. Shock propagation example

We consider a viscous gas undergoing uniaxial dynamic deformation in the direction of the X_1 axis. Then the motion may be fully described by a deformation mapping of the form $\varphi(X_1, X_2, X_3, t) = (\varphi_1(X_1, t), X_2, X_3)$. The corresponding deformation gradient is

$$F = \begin{pmatrix} \varphi_{1,1} & 0 & 0 \\ 0 & 1 & 0 \\ 0 & 0 & 1 \end{pmatrix}$$

with rate of deformation

$$d = \dot{F} F^{-1} = \begin{pmatrix} \dfrac{\dot{\varphi}_{1,1}}{\varphi_{1,1}} & 0 & 0 \\ 0 & 0 & 0 \\ 0 & 0 & 0 \end{pmatrix}$$

For simplicity, we assume that there are no body forces and that the material is homogeneous. Then, the action is of the form:

$$S(\varphi_1) = \int_{t_0}^{t_f} \int_{-\infty}^{\infty} \left(\frac{R}{2} \dot{\varphi}_1^2 - W(\varphi_{1,1}) \right) \mathrm{d}X \, \mathrm{d}t$$

where we assume the body to be unbounded in the X_1 direction. In this case, the equations of mechanical and configurational force balance reduce to

$$R \ddot{\varphi}_1 = P^e_{11,1} + P^v_{11,1} \tag{68}$$

$$R(-\varphi_{1,1}) \ddot{\varphi}_1 = C_{11,1} + (-\varphi_{1,1}) P^v_{11,1} \tag{69}$$

where P^e_{11} and C_{11} are, respectively, the equilibrium part of the first Piola–Kirchhoff stress and the dynamic Eshelby stress given by

$$P^e_{11} = \frac{\partial W}{\partial \varphi_{1,1}}$$

$$C_{11} = \left(W - \frac{R}{2} \dot{\varphi}_1^2 \right) - \varphi_{1,1} \frac{\partial W}{\partial \varphi_{1,1}}$$

DOI: 10.1002/nme

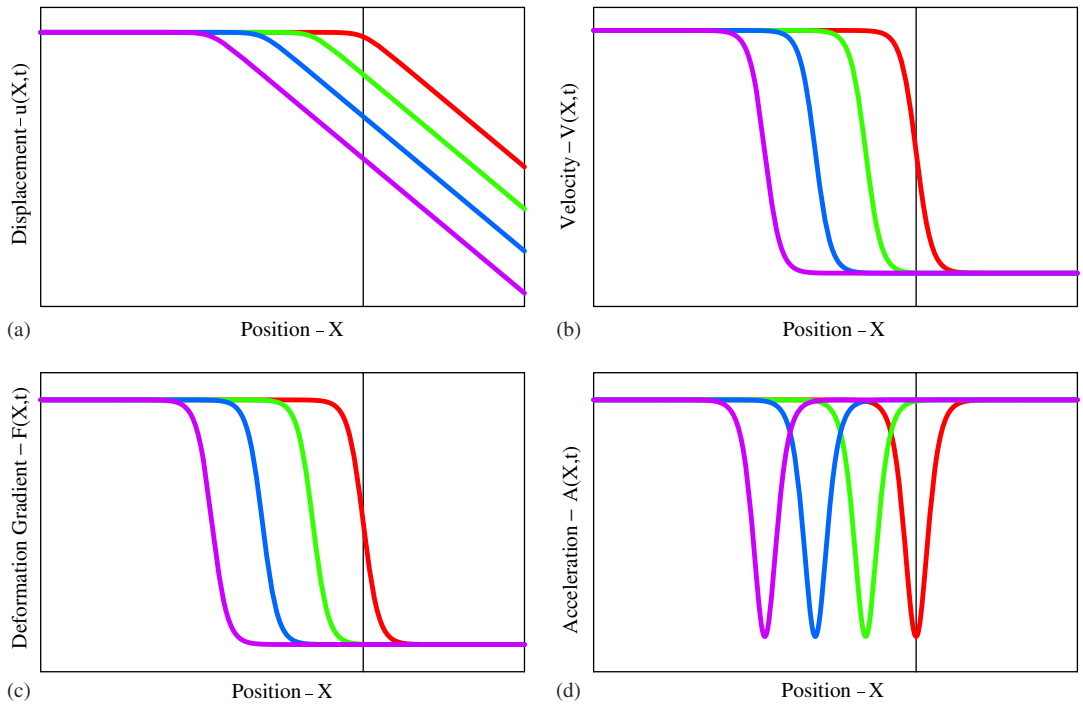

Figure 7. Propagation of a planar isothermal compression shock. Time evolution of (a) displacement, (b) velocity, (c) deformation gradient and (d) acceleration fields. Analytical solution.

and P^v_{11} is the viscous Newtonian stress, which in this one-dimensional case simplifies to

$$P^v_{11} = \frac{4}{3}\mu\frac{\dot{\varphi}_{1,1}}{\varphi_{1,1}}$$

where μ is the Newtonian viscosity of the gas.

We note that, owing to the presence of viscous stresses, (68) and (69) represent extensions of the formulation developed in the foregoing to dissipative continua. This extension can be effected in a straightforward manner by recourse to the Lagrange–d'Alembert principle. The interested reader is referred to [27] for details.

Inserting the previous into (68) and (69) leads to the governing equations:

$$R\ddot{\varphi}_1 = \left(\frac{\partial W}{\partial \varphi_{1,1}} + \frac{4}{3}\mu\frac{\dot{\varphi}_{1,1}}{\varphi_{1,1}}\right)_{,1}$$

$$\frac{\mathrm{d}}{\mathrm{d}t}(R(-\varphi_{1,1})\dot{\varphi}_1) = \left(\left(W - \frac{R}{2}\dot{\varphi}_1^w\right) - \varphi_{1,1}\frac{\partial W}{\partial \varphi_{1,1}}\right)_{,1} + (-\varphi_{1,1})\left(\frac{4}{3}\mu\frac{\dot{\varphi}_{1,1}}{\varphi_{1,1}}\right)_{,1}$$

DOI: 10.1002/nme

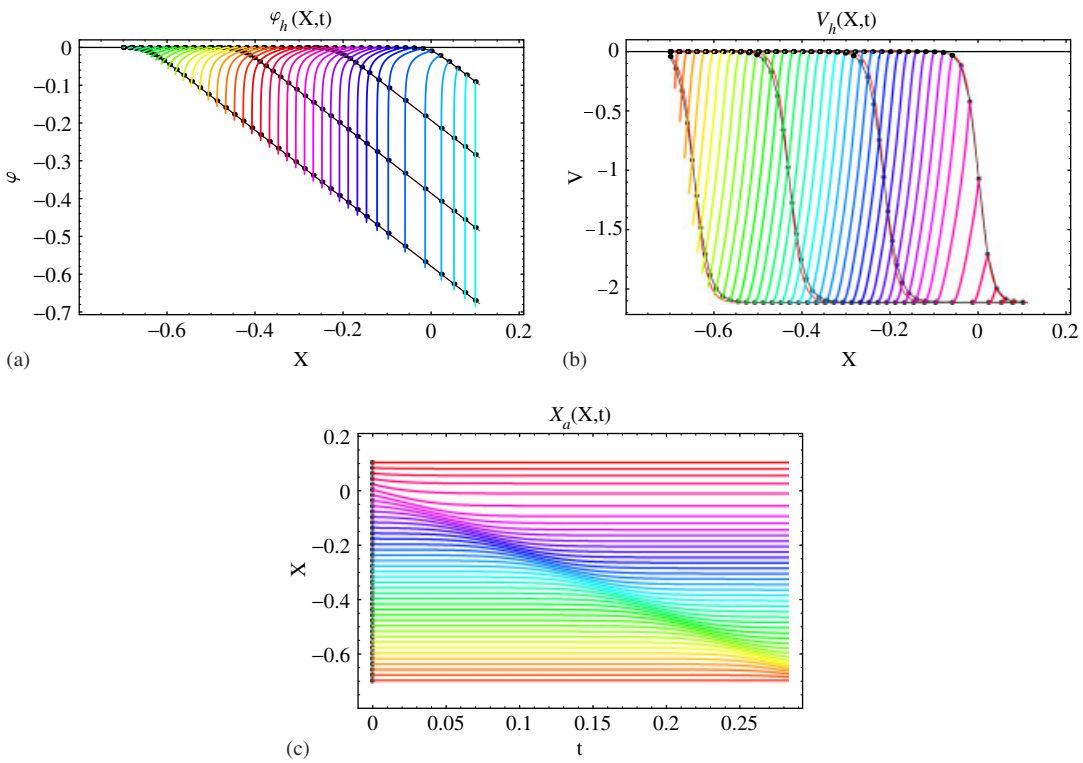

Figure 8. Time evolution of: (a) displacement; (b) velocity profile; and (c) nodal position in the reference configuration. Node trajectories and analytical solution are also displayed. The shock advances from right to left in the figure.

Remarkably, this problem admits exact analytical solutions for certain particular materials. A case in point is a gas characterized by the energy density:

$$W(J)=\frac{K}{4}(J^2-1-2\log(J))$$

where $J=\det(F)$. In this case, the analytical solution is of the form

$$\frac{\varphi_1(X_1,t)-X_1}{l}=f\left(\frac{X_1-ct}{l}\right)$$

where

$$f(\eta)=\left(\frac{J^+ + J^-}{2}-1\right)\eta+(J^+-J^-)\log\left(\frac{1}{2}\cosh\left(\frac{\eta}{2}\right)\right) \tag{70}$$

$$c^2=\frac{K}{2R}\left(1+\frac{1}{J^-J^+}\right) \tag{71}$$

$$l=\frac{8\mu c}{3K}\frac{J^-J^+}{J^+-J^-} \tag{72}$$

DOI: 10.1002/nme

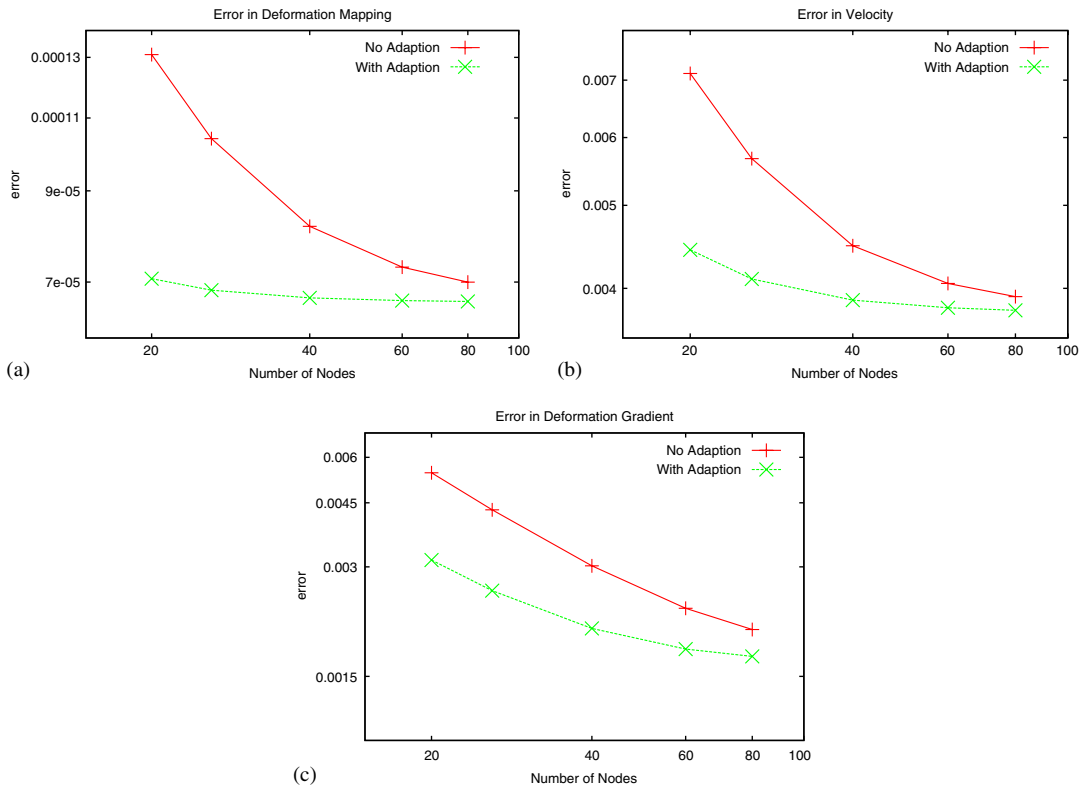

Figure 9. Convergence plot for isothermal compressive shock example: (a) displacement field; (b) velocity field; and (c) deformation gradient.

and J^+ and J^- are given boundary conditions:

$$J^{\pm} = \lim_{X_1 \to \pm\infty} \varphi_{1,1}(X_1, t)$$

The velocity field is given by

$$\dot{\varphi}_1 = -cf'\left(\frac{X_1 - ct}{l}\right)$$

where

$$f'(\eta) = \left(\frac{J^+ + J^-}{2} - 1\right) + \frac{J^+ - J^-}{2}\tanh\left(\frac{\eta}{2}\right)$$

The analytical solution for the displacement $u_1 = \varphi_1 - X_1$, velocity $\dot{\varphi}_1$, deformation gradient $\varphi_{1,1}$ and acceleration fields $\ddot{\varphi}_1$ is shown in Figure 7 for the following parameters: $R = 1$, $K = 1$, $\mu = 0.025$, $J^- = 1$, $J^+ = 0.1$. The corresponding shock velocity is $c = \sqrt{5.5} \simeq 2.3452$, and the shock thickness is $l = 1.7372 \times 10^{-2}$.

DOI: 10.1002/nme

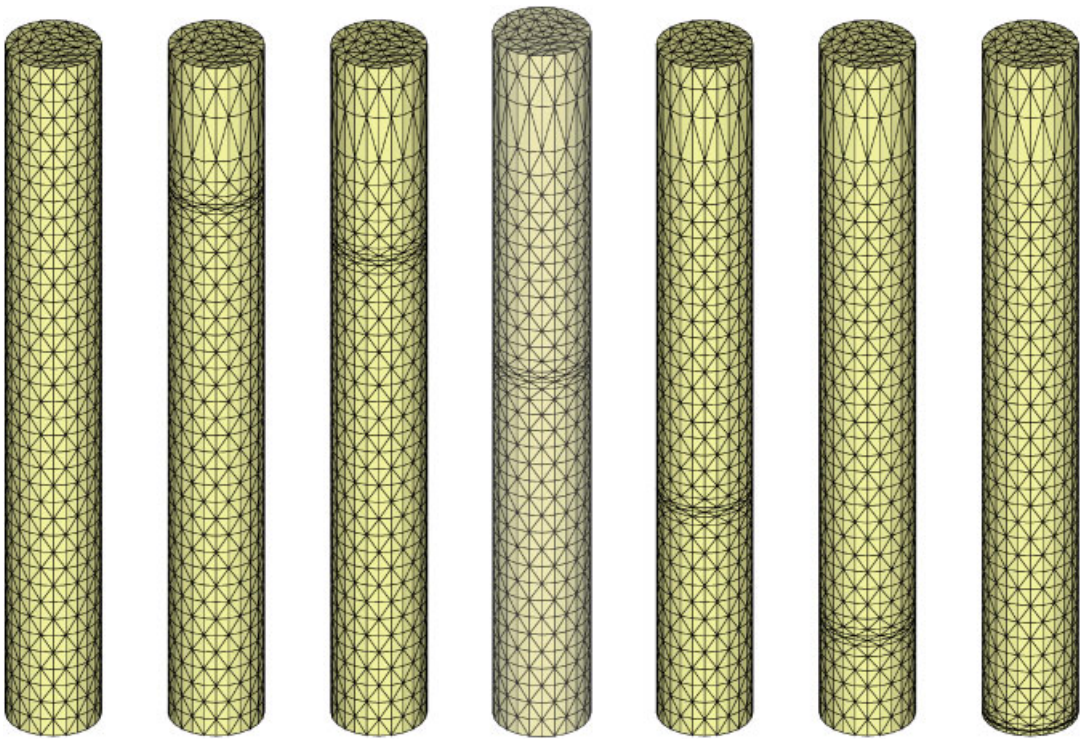

Figure 10. Propagation of a compression wave down a cylinder. Adapted 3D meshes at different times. Reference configuration.

We solve the problem numerically in one and three dimensions. The domain of analysis is discretized using linear elements in one dimension and four-noded linear tetrahedral elements in three dimensions. The governing equations are discretized in time using the mixed variational integrator described in Section 5 with integration parameter $\alpha = \frac{1}{2}$. The resulting system of non-linear equations for the update of referential and spatial nodal coordinates is solved using the Polak–Ribiere variant of the non-linear conjugate-gradient method. The stable time step is estimated as $\Delta t \leqslant h_{\min}/c$, where $h_{\min}$ is the minimum element size and c is the shock velocity. The length of the domain of analysis is $L = 70l$ or 70 times the width l of the shock.

The time evolution of the displacement and velocity fields and of the nodes in the reference configuration computed from the one-dimensional example is shown in Figures 8(a)–(c), respectively. In Figure 8(a) and (b), the node trajectories and the exact solution are also shown for reference. It is remarkable how nodes cluster through the shock front, thus providing the optimal (in the sense of the action) resolution of the shock structure permitted by the number of nodes in the calculation. The smoothness and non-dispersive qualities of the computed solution are also noteworthy. The later property is evidenced by the nearly steady translation of the shock profile. It is also evident from the figures that the shock velocity is well captured by the numerical solution. It bears emphasis that this performance is obtained without the use of artificial viscosity or other shock-capturing techniques.

DOI: 10.1002/nme

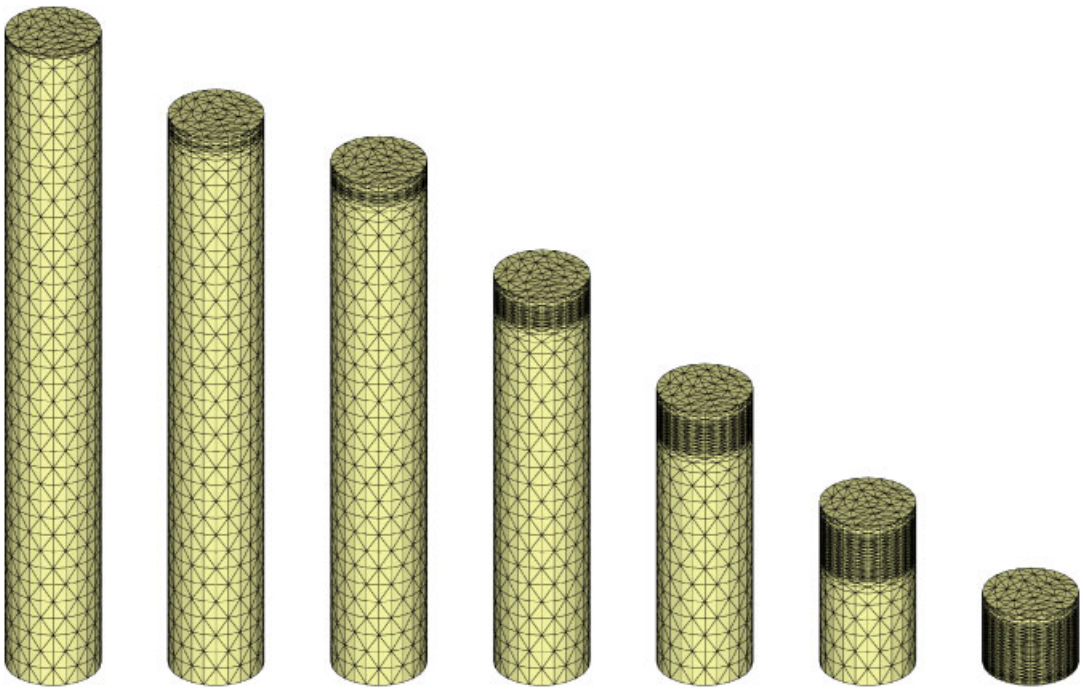

Figure 11. Propagation of a compression wave down a cylinder. Adapted 3D meshes at different times. Deformed configuration.

Figure 9 shows computed convergence curves for the one-dimensional solution expressed in terms of the $L_2(B \times [t_0, t_f])$-norm of the difference between the analytic and finite element displacement, velocity and deformation-gradient fields. These errors are plotted against the number of degrees of freedom in a log–log axis. As is evident from Figure 9, the gain in accuracy afforded by adaption is quite considerable for coarse meshes, less so for fine meshes.

Figures 10 and 11 show a sequence of snapshots of the adapted mesh during the three-dimensional simulation in both reference and the deformed configurations. It can be observed that the nodes cluster in the neighborhood of the shock front and follow the shock as it propagates along the domain. The motion of the nodes relative to the material is most clearly shown in Figure 10. The large size of the deformations, which are well into the finite kinematics range, is strikingly evident in Figure 11. As noted in the Introduction, even when regularity can be counted on, meaningful and tight error bounds for dynamical, dissipative and strongly non-linear problems, such as the present example are not likely to ever be available in general. In view of this essential difficulty, the ability of the variational approach to deliver high-quality adaptivity under those conditions is all the more remarkable.

Figure 12 depicts the evolution of the velocity profile computed from the three-dimensional mesh on a plane containing the axis of the cylinder. As in the one-dimensional case, the smoothness of the profiles, obtained without the use of artificial viscosity or any other shock-stabilization tricks, and the absence of dispersion, as evidenced by the steady translation of the computed profile, are quite remarkable.

DOI: 10.1002/nme

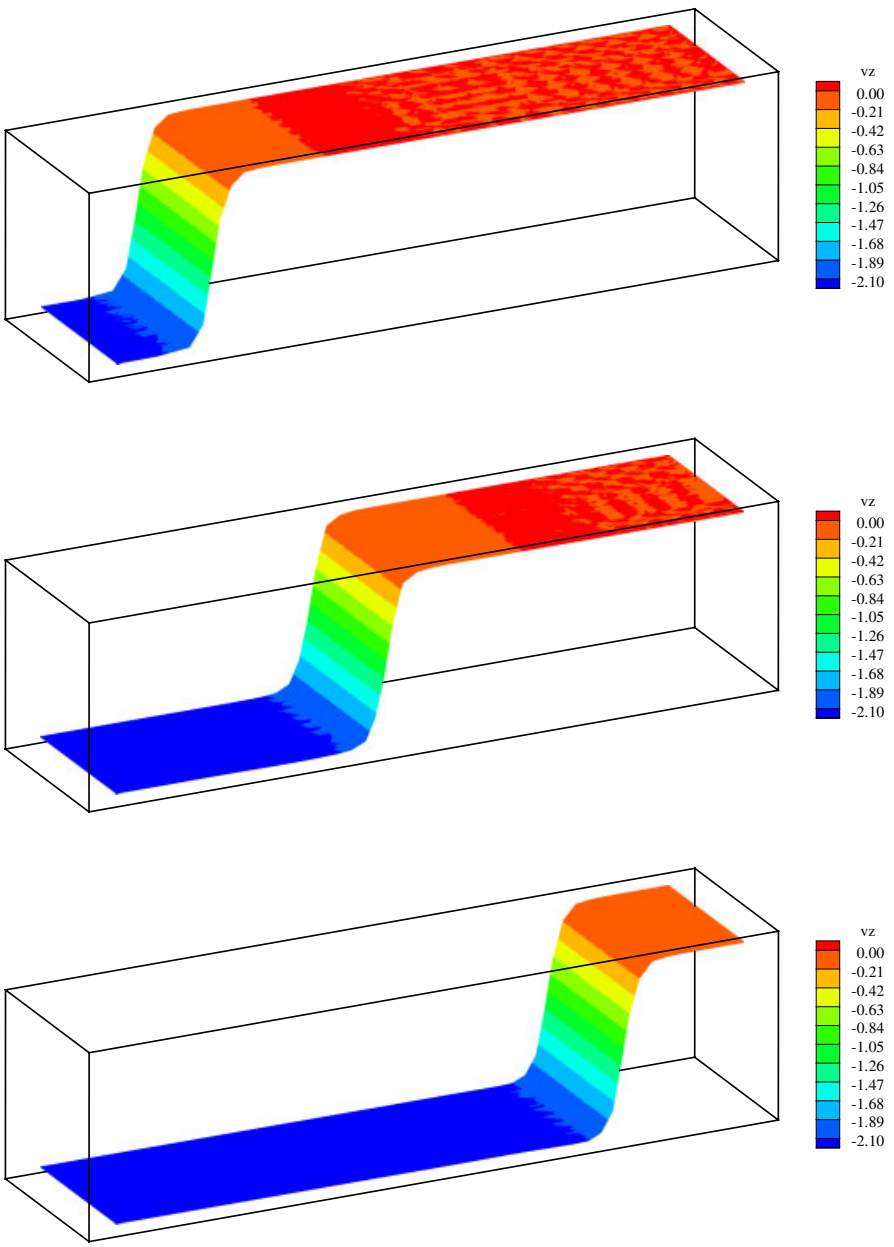

Figure 12. Profile and contour plot of axial velocity at different times of the simulation on a plane that contains the axis of the cylinder.

An interesting variation in the present example concerns a shock tube with an abrupt change in its cross section. A shock wave is introduced at the narrow end of the tube. The material and material parameters are identical to those used in the preceding calculations. Figure 13 shows

DOI: 10.1002/nme

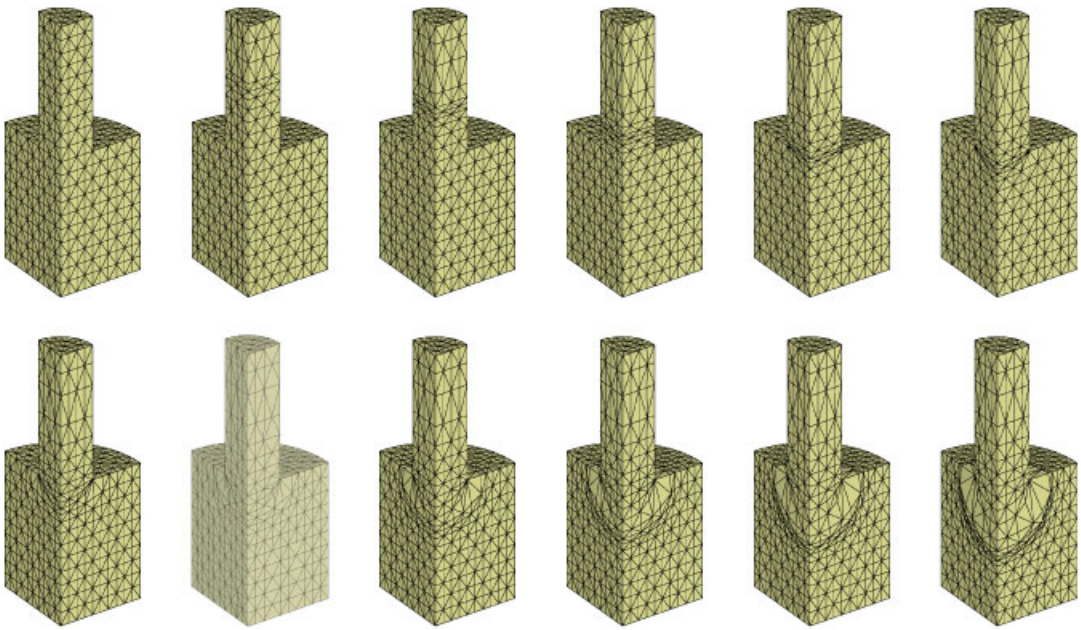

Figure 13. Propagation of a plane wave down a cylinder with a sudden expansion. Snapshots of the instantaneous mesh (in the reference configuration) at different time steps.

a sequence of snapshots of the evolution of the adapted mesh in the reference configuration at different times. As is evident from the figure, the mesh, while coarse, does track the gross motion of the shock as it turns the corner in the cross section and bows into the wide part of the shock tube. Again, the ability of the method to adapt to rapidly changing transients and complex spatial patterns in the solution is noteworthy. This ability notwithstanding, it is also clear from this example that in order to accurately resolve the full structure of the corner-turning solution r-adaption must be combined with h-adaption, or adaptive mesh refinement and unrefinement. For static problems, variational hr-adaption schemes have been discussed in [52].

6.2. Neohookean block under a moving point load

Our next example concerns a three-dimensional elastic block deforming under the action of a moving point load applied to its surface. The block dimensions are $1\times1\times0.5$ and zero normal displacement boundary conditions are enforced on the base and on the face closest to the initial point of application of the load. Only half of the block is simulated due to the symmetry of the loads and geometry. The material is Neohookean extended to the compressible level and is characterized by the strain-energy density:

$$W(X,F)=\frac{\lambda_0(X)}{2}\log(\det(F))^2-\mu_0(X)\log(\det(F))+\frac{\mu_{0(X)}}{2}\operatorname{tr}(F^{\mathrm{T}}F)$$

where λ_0 and μ_0 are Lame constants. In calculations, the Lame constants are given the values: $\lambda_0=1.73\times10^6$ and $\mu_0=10^6$ corresponding to a Poisson ratio $v_0=0.3$. The mass density per unit of undeformed volume is $R=100$. The load moves at $\frac{1}{10}$ of the undeformed shear wave speed

DOI: 10.1002/nme

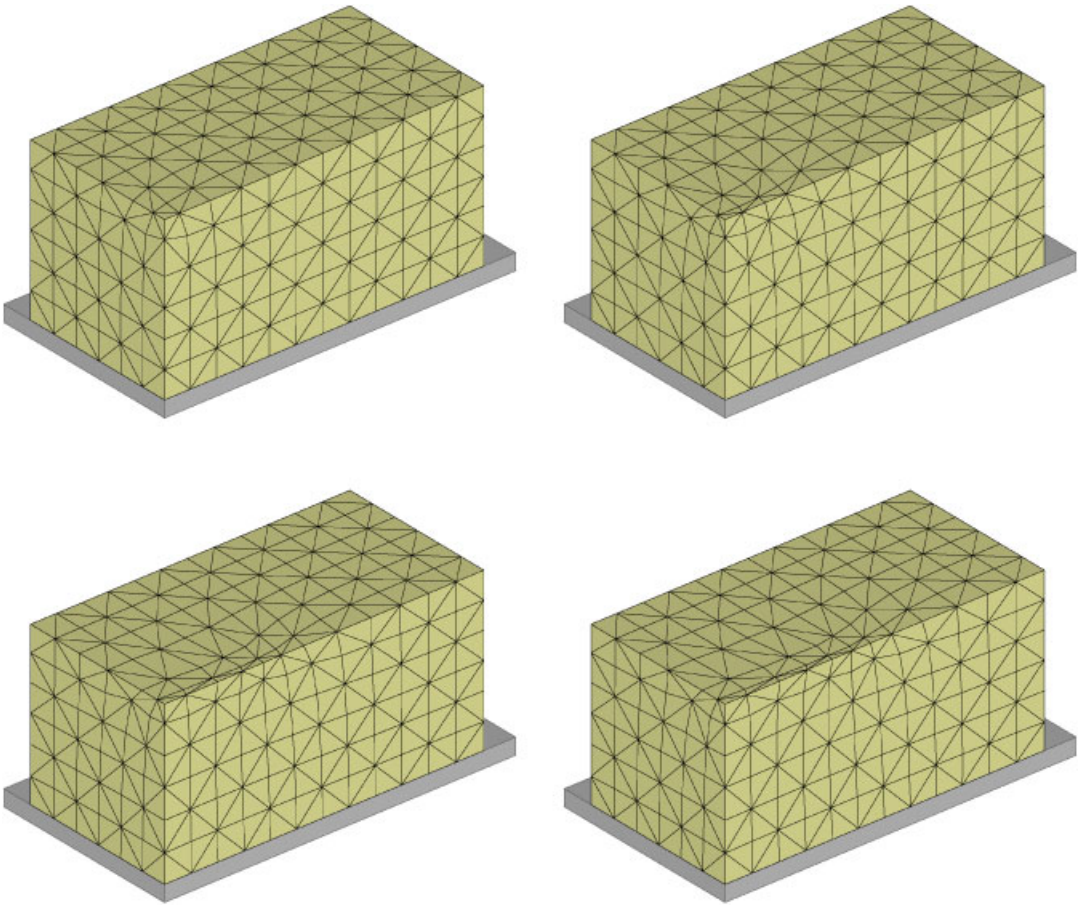

Figure 14. Neohookean block subjected to a moving point load. Reference configuration and adapted mesh at different times of the simulation.

of the material. The mesh consists of 2160 tetrahedral linear finite elements and 637 nodes. In order to maintain the geometry of the block during the computation, the motion of the nodes within the reference configuration is constrained so that each face node remains within its face and each edge node remains within its edge and. The vertex nodes are not allowed to move in the reference configuration. Figure 14 shows snapshots of the adapted mesh at different times during the simulation. Figure 15 shows the deformed configuration, the adapted mesh and contour plot of the vertical displacement. As expected, the nodes tend to cluster near the point of application of the load. It is also noteworthy that the mesh is too coarse to resolve the elastic waves radiated from the moving point load. Indeed, an examination of the configurational forces reveals that the static contribution to these forces greatly outweighs the dynamic contribution. As a result, in this case the clustering of the nodes closely matches that which would arise under statics conditions.

DOI: 10.1002/nme

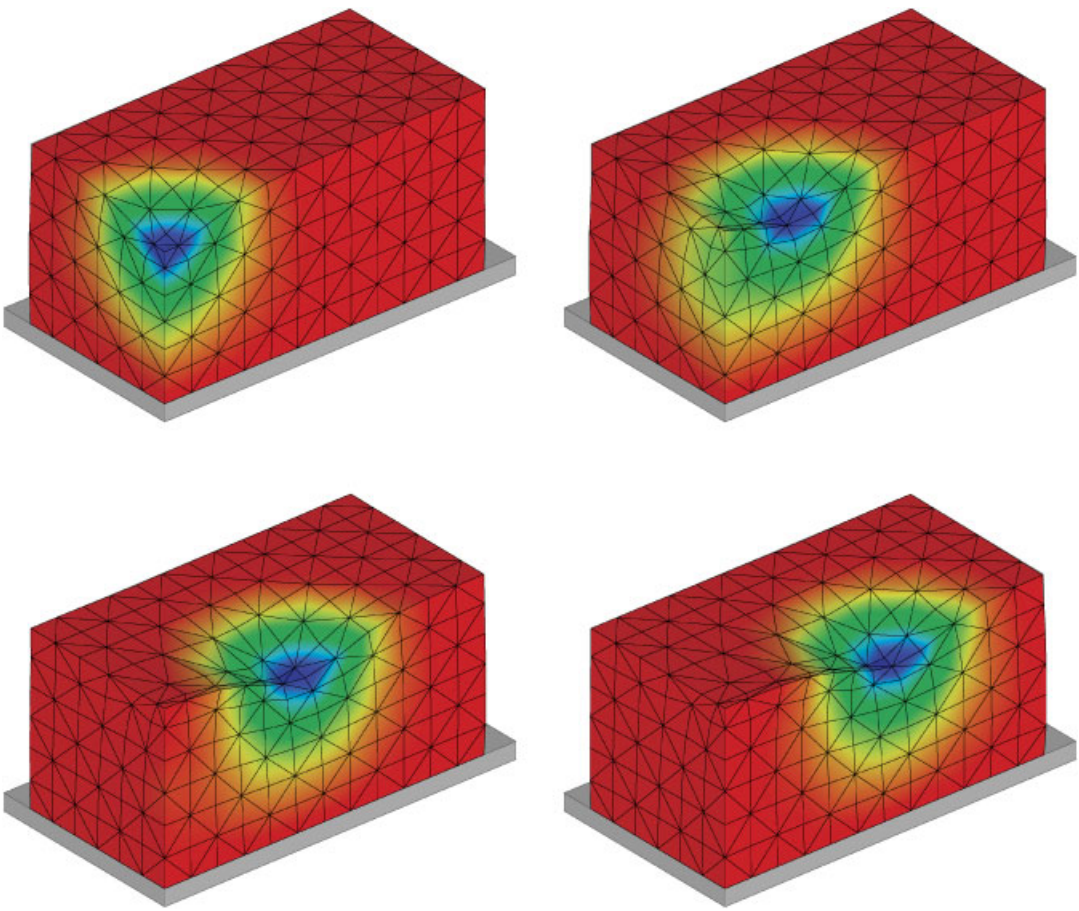

Figure 15. Neohookean block subjected to a moving point load. Adapted mesh in the deformed configuration at different times of the simulation and contour plot of vertical displacements.

6.3. Crack propagation example

Our final example concerns the dynamic propagation of a mode I crack in a square plate, Figure 16. Owing to the symmetry of the geometry and loading, only the upper half of the body is simulated. As in the preceding example, the motion of the surface nodes is constrained so as to preserve the geometry of the plate. The material is compressible Neohookean with Lame constants $\lambda_0 = 1.73 \times 10^6$ and $\mu_0 = 10^6$, and the mass density per unit undeformed volume is $R = 2300$. The mesh consists of 720 linear tetrahedral finite elements and 273 nodes. Displacement boundary conditions corresponding to a linear elastic K_I-field are applied to the boundary for a stress-intensity factor $K_I = 1E^5$. The crack front is advanced by assuming a constant crack tip velocity equal to $\frac{1}{10}$ of the undeformed shear wave speed of the material. In order to simulate the crack advance, nodes on the crack plane are released when the nominal crack front reaches the downstream nearest-neighbor node. Figure 17 shows the adapted mesh within the reference configuration at different times during the simulation. Figure 18 shows the adaptive mesh in the deformed configuration

DOI: 10.1002/nme

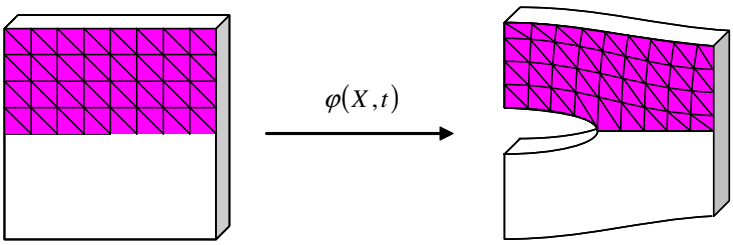

Figure 16. Dynamic propagation of a crack along a slab of Neohookean material: (a) reference configuration and (b) schematic of deformed configuration at time t.

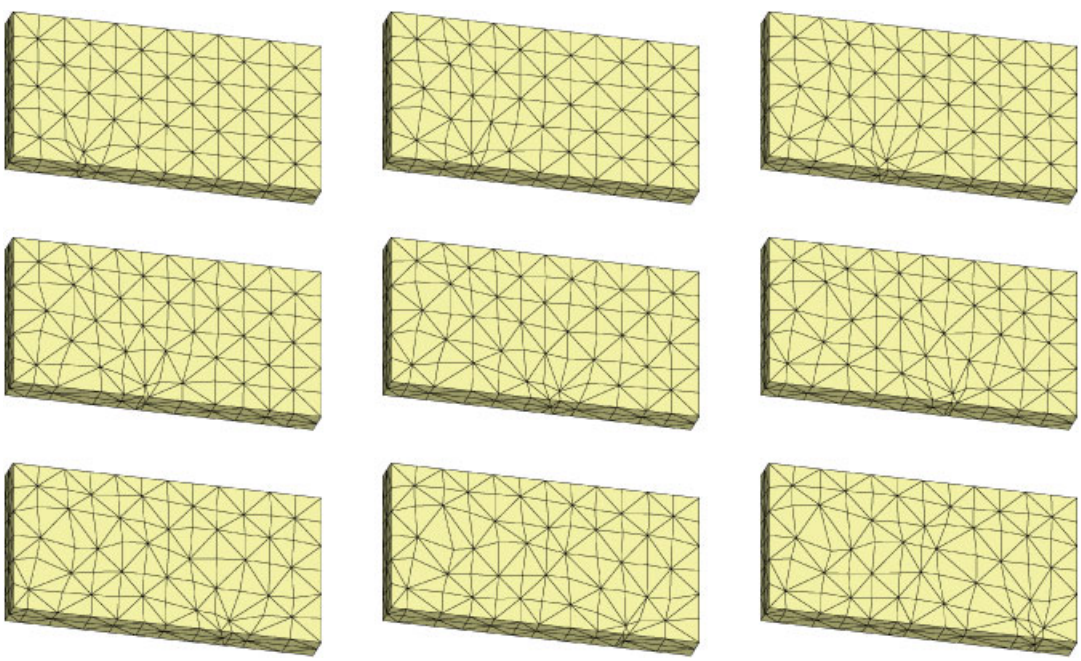

Figure 17. Propagation of a crack along a slab of Neohookean material. Adapted mesh in the reference configuration at different time steps of the simulation.

and contour plots of vertical displacement. As expected, nodes tend to cluster near the moving crack tip. A close examination of the solution reveals that the nodes also move in an oscillatory fashion so as to facilitate the radiation of elastic waves from the crack tip. This example again illustrates that the motion of the nodes is sensitive to the detailed spatial and transient structure of the solution, including moving singularities and elastic waves.

DOI: 10.1002/nme

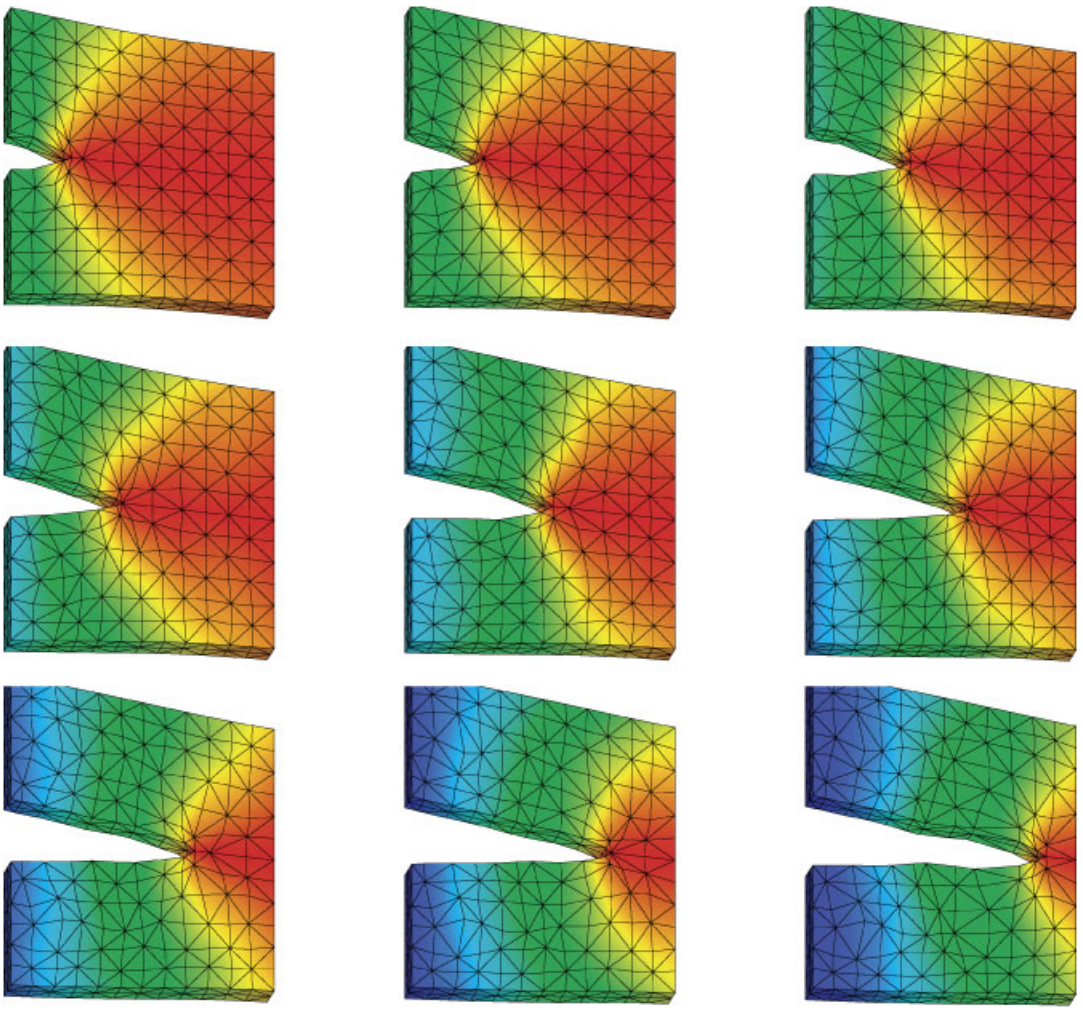

Figure 18. Crack propagation along a Neohookean body. The nodes cluster following the crack tip. Contour plots indicate vertical displacements.

7. CONCLUDING REMARKS

We have developed a variational finite element mesh adaption framework for solid dynamic applications and its conceptual links with the theory of dynamic configurational forces. A mixed, multifield version of Hamilton's principle and a mixed extended version of Lagrange–d'Alembert principle are proposed as underlying variational principles for the formulation. Additional building blocks include: the use of uncoupled space and time discretizations; the use of independent space interpolations for velocities and deformations; the application of these interpolations over a continuously varying adaptive mesh; and the application of mixed variational integrators with

DOI: 10.1002/nme

independent time interpolations for velocities and nodal parameters. The result is a robust adaptive finite element formulation for dynamic applications that satisfies balance of mechanical forces (or balance of spatial momentum) and the balance of dynamic configurational forces (or balance of material momentum). In addition, owing to their variational nature the solutions exhibit excellent long-term stability behavior.

It bears additional emphasis that the need to adopt a mixed formulation stems from the unstable behavior that results from a direct consistent or Galerkin discretization of the classical action. After careful examination and testing, it is concluded that these instabilities are caused by the inaccuracy of the consistent velocity field, and in particular by its discontinuous nature. Remarkably, this unstable behavior is eliminated when a mixed multifield version of Hamilton's principle is adopted.

Whereas the focus of this paper is the development of numerical algorithms in the context of elastodynamics, the general framework can be extended to include viscosity, transport phenomena, such as heat conduction, and inelastic behavior, such as plasticity. A detailed exposition of these extensions may be found in [27]. The inclusion of viscosity in the formulation is accomplished within the framework of the Lagrange–d'Alembert principle. Here again, the stability of the solutions requires the formulation of a mixed multifield version of this principle. Heat conduction may be given a variational structure through the use of *thermal displacements* [44, 53–57], in place of temperature, as the fundamental thermal field. By recourse to this representation, the heat flux possesses a structure that is in analogy to the equilibrium/viscous additive decomposition of stress and that can, therefore, be given a similar treatment within the Lagrange–d'Alembert framework. A comprehensive treatment of configurational forces in the presence of viscosity, heat conduction and inelasticity may be found in [27].

In this paper, we have eschewed all geometrical aspects of the mixed Hamilton principle in favor of numerical issues. Some of these geometrical aspects are analyzed in detail in [27]. Suffice it to say here that, while not obvious from their form, the joint equations of mechanical and configurational momentum balance define a flow on a *constraint manifold* that links the motion of the nodes in the reference and deformed configurations. This constrained manifold may be regarded as a submanifold of the material–spatial product configuration manifold. For instance, in the one-dimensional example of Section 2.1, the constraint manifold is defined by Equation (18). No such constraint manifold exists for naive consistent discretizations of the action. The geometrical structure of the mixed dynamical system provides considerable insight into the properties of the solutions. In particular, the good stability properties of the solution may be traced to the existence of a constrained manifold.

APPENDIX A: CALCULATION OF THE CONSISTENT VELOCITY FIELD

Differentiation of (47) with respect to time t yields the identity

$$\dot{\varphi}^e(X,t)=\sum_{a=1}^{n}(N_a^e(X,t)\dot{x}_a^e(t)+\dot{N}_a^e(X,t)\dot{x}_a^e(t)) \tag{A1}$$

where a superposed dot denotes partial differentiation with respect to time. In order to evaluate the rate $\dot{N}_a^e$, we resort to the isoparametric representation of the shape functions and express

$$N_a^e(\psi^e(\xi,t),t)=\hat{N}_a(\xi) \tag{A2}$$

DOI: 10.1002/nme

Differentiation of this identity with respect to time gives

$$\frac{\partial N_a^e}{\partial t}\circ\psi^e+\left(\frac{\partial N_a^e}{\partial X_I}\circ\psi^e\right)\dot{\psi}_I^e=0 \tag{A3}$$

whereas differentiation of (48a) gives

$$\dot{\psi}_I^e(\xi,t)=\sum_{a=1}^{n}\hat{N}_a(\xi)\dot{X}_{aI}^e(t) \tag{A4}$$

From these identities, we find

$$\frac{\partial N_a^e}{\partial t}\circ\psi^e=-\left(\frac{\partial N_a^e}{\partial X_I}\circ\psi^e\right)\sum_{a=1}^{n}\hat{N}_a(\xi)\dot{X}_{aI}^e \tag{A5}$$

which, after composition with ψ^{e-1} and use of relation (48a), yields the identity

$$\frac{\partial N_a^e}{\partial t}=-\frac{\partial N_a^e}{\partial X_I}\sum_{a=1}^{n}N_a^e\dot{X}_{aI}^e \tag{A6}$$

Inserting this identity into (A1) further gives

$$\begin{aligned}\dot{\varphi}_i^e(X,t)&=\sum_{a=1}^{n}N_a^e\dot{x}_{ai}^e-\left(\sum_{a=1}^{n}\frac{\partial N_a^e}{\partial X_I}x_{ai}^e\right)\sum_{b=1}^{n}N_b^e\dot{X}_{bI}^e\\&=\sum_{a=1}^{n}N_a^e\dot{x}_{ai}^e-F_{iI}^e\sum_{b=1}^{n}N_b^e\dot{X}_{bI}^e\\&=\sum_{a=1}^{n}N_a^e(\dot{x}_{ai}^e-F_{iI}^e\dot{X}_{aI}^e)\end{aligned} \tag{A7}$$

where

$$F_{iI}^e(X,t)=\sum_{a=1}^{n}x_{ai}^e(t)\frac{\partial N_a^e}{\partial X_I}(X,t) \tag{A8}$$

is the local deformation gradient field.

ACKNOWLEDGEMENTS

Support of the Department of Energy through Caltech's ASCI/ASAP Center for Simulating the Dynamic Response of Materials and NSF-ITR Grant ACI-0204932 is gratefully acknowledged.

REFERENCES

1. Radovitzki R, Ortiz M. Error estimation and adaptive meshing in strongly non-linear dynamic problems. *Computer Methods in Applied Mechanics and Engineering* 1999; **172**(1–4):203–240.

DOI: 10.1002/nme

2. McNiece GM, Marcal PM. Optimization of finite element grids based on minimum potential energy. *Transaction of the ASME* 1976; **1**:186–190.
3. Felippa C. Optimization of finite element grids by direct energy search. *Applied Mathematical Modelling* 1976; **1**:93–96.
4. Felippa C. Numerical experiments in finite element grid optimization by direct energy search. *Applied Mathematical Modelling* 1977; **1**:239–244.
5. Eshelby JD. The force on an elastic singularity. *Philosophical Transactions of the Royal Society of London* 1951; **244**:87–112.
6. Eshelby JD. The elastic Eshelby momentum tensor. *Journal of Elasticity* 1975; **5**:321–335.
7. Braun M. Configurational forces induced by finite element discretization. *Proceedings of the Estonian Academy of Sciences*, *Physics*, *and Mathematics* 1997; **46**:24–31.
8. Mueller R, Maugin GA. On material forces and finite element discretizations. *Computational Mechanics* 2002; **29**:52–60.
9. Mueller R, Kolling S, Gross D. On configurational forces in the context of the finite element method. *International Journal for Numerical Methods in Engineering* 2002; **53**:1557–1574.
10. Thoutireddy P. Variational arbitrary Lagrangian–Eulerian method. *Ph.D. Thesis*, California Institute of Technology, 2003. Available at: http://etd.caltech.edu/etd/available/etd-05292003-113845/.
11. Thoutireddy P, Ortiz M. A variational r-adaption and shape-optimization method for finite-deformation elasticity. *International Journal for Numerical Methods in Engineering* 2004; **61**:1–21.
12. Mueller R, Gross D, Maugin GA. Use of material forces in adaptive finite element methods. *Computational Mechanics* 2004; **33**:421–434.
13. Kuhl E, Askes H, Steinman P. An ALE formulation based on spatial and material settings of continuum mechanics. Part 1: generic hyperelastic formulation. *Computer Methods in Applied Mechanics and Engineering* 2004; **193**:4203–4222.
14. Kuhl E, Steinmann P. A hyperelastodynamic ALE formulation based on referential, spatial and material settings of continuum mechanics. *Acta Mechanica* 2005; **174**:201–222.
15. Askes H, Kuhl E, Steinman P. An ALE formulation based on spatial and material settings of continuum mechanics. Part 2: classification and applications. *Computer Methods in Applied Mechanics and Engineering* 2004; **193**:4223–4245.
16. Mosler J, Ortiz M. On the numerical implementation of variational arbitrary Lagrangian–Eulerian (VALE) formulations. *International Journal for Numerical Methods in Engineering* 2006; **67**:1272–1289.
17. Lew A. Variational time integrators in computational solid mechanics. *Ph.D. Thesis*, California Institute of Technology, 2003. Available at: http://etd.caltech.edu/etd/available/etd-05262003-200254/.
18. Lew A, Marsden JE, Ortiz M, West M. Asynchronous variational integrators. *Archive for Rational Mechanics and Analysis* 2003; **167**:85–146.
19. Lew A, Marsden JE, Ortiz M, West M. Variational time integrators. *International Journal for Numerical Methods in Engineering* 2002; **3**:1–10.
20. West M. Variational integrators. *Ph.D. Thesis*, California institute of technology, 2004. Available at: http://etd.caltech.edu/etd/available/etd-06072004-161416/0.
21. Leok M. Foundations of computational geometric mechanics. *Ph.D. Thesis*, California Institute of Technology, 2004. Available at: http://etd.caltech.edu/etd/available/etd-03022004-000251/.
22. Pontryagin LS, Boltyanskii VG, Gamkrelidze RV, Mishchenko EF. *The Mathematical Theory of Optimal Processes*. Wiley: New York, 1962.
23. Yoshimura H, Marsden JE. Dirac structures in Lagrangian mechanics. Part II: variational structures. *Journal of Geometry and Physics* 2006; **57**:209–250.
24. Kharevych L, Tong WY, Kanso E, Marsden JE, Schröder P, Desbrun M. Geometric, variational integrators for computer animation. *Eurographics ACM SIGGRAPH Symposium on Computer Animation*, Vienna, Austria, 2006; 1–9.
25. Washizu K. *Variational Methods in Elasticity and Plasticity* (3rd edn). International Series of Monographs in Aeronautics and Astronautics: Solid and Structural Mechanics, vol. 9. Pergamon Press: Oxford, 1982.
26. Felippa C. On the original publication of the general canonical functional of linear elasticity. *Journal of Applied Mechanics* 2000; **67**:217–219 (Brief notes).
27. Zielonka MG. Configurational forces and variational mesh adaption in solid dynamics. *Ph.D. Thesis*, California Institute of Technology, 2006. Available at: http://etd.caltech.edu/etd/available/etd-05112006-162905/.
28. Truesdell CA, Noll W. The non-linear field theories of mechanics. *Flügge's Handbuch der Physik*, vol. 3, Part 3. Springer: Berlin, 1965 (2nd edn, corrected, 1992).

DOI: 10.1002/nme

29. Lodge AS. On the use of convected coordinate systems in the mechanics of continuous media. *Proceedings of the Cambridge Philosophical Society* 1951; **47**:575.
30. Yavari A, Marsden JE, Ortiz M. On spatial sand material covariant balance laws in elasticity. *Journal of Mathematical Physics* 2006; **47**:1–53.
31. Maugin GA. *Material Inhomogeneities in Elasticity*. Chapman & Hall: London, 1993.
32. Maugin GA. 'Material' mechanics of materials. *Theoretical and Applied Mechanics* 2002; **27**:1–12.
33. Maugin GA. Recent advances in M^3 (mechanics on the material manifold). *Theoretical and Applied Mechanics* 2002; **28–29**:221–233.
34. Maugin GA. Material forces: concepts and applications. *Applied Mechanics Reviews* 1995; **48**(5):213–245.
35. Noll W. Materially uniform simple bodies with inhomogeneities. *Archive for Rational Mechanics and Analysis* 1967; **27**:1–32.
36. Epstein M, Maugin GA. The energy–momentum tensor and material uniformity in finite elasticity. *Acta Mechanica* 1990; **83**:127–133.
37. Epstein M, Maugin GA. On the geometrical material structure of anelasticity. *Acta Mechanica* 1996; **115**: 119–131.
38. Epstein M. The Eshelby tensor and the theory of continuous distribution of inhomogeneities. *Mechanics Research Communications* 2002; **29**:501–506.
39. Maugin GA, Epstein M. Geometrical material structure of elastoplasticity. *International Journal of Plasticity* 1998; **14**:109–115.
40. Maugin GA. Pseudo-plasticity and pseudo-inhomogeneity effects in materials mechanics. *Journal of Elasticity* 2003; **71**:81–103.
41. Cermelli P, Fried E. The influence of inertia on the configurational forces in a deformable solid. *Proceedings of the Royal Society of London*, *Series A* 1997; **453**:1915–1927.
42. Gurtin ME. The nature of configurational forces. *Archive for Rational Mechanics and Analysis* 1995; **131**:67–100.
43. Gurtin ME. *Configurational Forces as Basic Concepts of Continuum Physics*. Applied Mathematical Sciences, vol. 137. Springer, 2000.
44. Kalpakides VK, Dascalu C. On the configurational force balance in thermomechanics. *Proceedings of the Royal Society of London*, *Series A* 2002; **458**:3023–3039.
45. Knowles JK, Sternberg E. On a class of conservation laws in linearized and finite elastostatics. *Archive for Rational Mechanics and Analysis* 1971; **44**:187–211.
46. Marsden JE, Hughes TJR. *Mathematical Foundations of Elasticity*. Prentice-Hall: Englewood Cliffs, NJ, 1983.
47. Kienzler R, Herrmann G. *Mechanics in Material Space with Applications to Defect and Fracture Mechanics*. Springer: Germany, 2000.
48. Maugin G, Trimarco C. Pseudo quantite de mouvement et milieux elastiques inhomogenes. *Comptes Rendus de l'Académie Sciences Serie II* 1991; **313**:851–856.
49. Podio-Guidugli P. Configurational balances via variational arguments. *Interfaces and Free Boundaries* 2001; **3**:1–10.
50. Steinmann P. On spatial and material settings of thermo-hyperelastodynamics. *Journal of Elasticity* 2002; **66**(2):109–157.
51. Kane C, Marsden JE, Ortiz M. Symplectic-energy–momentum preserving variational integrators. *Journal of Mathematical Physics* 1999; **40**(7):3353–3371.
52. Mosler J, Ortiz M. Variational h-adaption in finite deformation elasticity and plasticity. *International Journal for Numerical Methods in Engineering* 2007; **72**(5):505–523.
53. Green AE, Naghdi PM. A re-examination of the basic postulates of thermomechanics. *Proceedings of the Royal Society of London*, *Series A* 1991; **432**:171–194.
54. Maugin GA. Towards an analytical mechanics of dissipative materials. *Rendiconti del Seminario Matematico*, vol. 58(2). Geometry, Continua and Microstuctures. Universita e Politecnico di Torino, Torino, 2000.
55. Maugin GA, Kalpakides VK. A Hamiltonian formulation for elasticity and thermoplasticity. *Journal of Physics A—Mathematical and General* 2002; **35**:10775–10788.
56. Kalpakides VK, Maugin GA. Canonical formulation and conservation laws of theromelasticity without dissipation. *Reports on Mathematica Physics* 2004; **53**(3):371–391.
57. Dascalu C, Maugin GA. The thermoelastic material–momentum equation. *Journal of Elasticity* 1995; **39**:201–212.

DOI: 10.1002/nme